Design of Functional Composite and All–inorganic Nanostructured Materials via Infiltration of Polymer Templates with Inorganic Precursors

Journal:	*Journal of Materials Chemistry C*
Manuscript ID	TC-REV-01-2020-000483.R1
Article Type:	Review Article
Date Submitted by the Author:	15-Mar-2020
Complete List of Authors:	Berman, Diana; University of North Texas, Materials Science and Engineering Shevchenko, Elena; Argonne National Laboratory, Center for Nanoscale Materials

SCHOLARONE™
Manuscripts

Design of Functional Composite and All-inorganic Nanostructured Materials via Infiltration of Polymer Templates with Inorganic Precursors

Diana Berman[1], Elena Shevchenko[2]

[1] Materials Science and Engineering Department, University of North Texas, Denton, Texas, 76203, United States

[2] Nanoscience and Technology Division, Argonne National Laboratory, Argonne, Illinois 60439, United States

*Corresponding authors: Diana Berman (diana.berman@unt.edu), Elena Shevchenko (eshevchenko@anl.gov)

Abstract

Robust and efficient approaches for the synthesis of materials with structure, porosity, and composition controlled at the nanoscale are highly important for a wide range of applications. Polymer templates are promising platforms to achieve such control. The self-assembly process of polymers provides access to diverse structures that can serve as templates for the deposition of inorganic materials. By infiltrating metal precursors from gas or liquid phases, using sequential infiltration synthesis (SIS) or swelling-based infiltration (SBI), respectively, into the polymer templates, one can create finely-tuned texturing of the surface films and bulk materials. In this review, we outline the specifics and dynamics of the polymer infiltration process and characterize the structure and properties of the synthesized materials. Finally, we highlight recent progress in implementing polymer infiltration-based nanoporous ceramics for many applications, including sensors, antireflective coatings, oil-absorbing foams, nanolithographic patterns, and catalytic materials.

Keywords

Polymer templates, polymer infiltration, block copolymer, nanoporous ceramics, lateral coatings, sequential infiltration synthesis,

1. Introduction

Polymer assemblies are recognized as promising platforms for the design of a broad range of functional composite and all-inorganic structures [1-4]. There are three critical parameters that make the use of polymer templates appealing for the design of functional materials. First, the polymer chains can carry functional groups serving as reaction centers enabling the synthesis of the inorganic nanostructures. Second, the polymer can create a "mold" that defines the pattern for inorganic structures. In particular, the ability to manipulate the structure of the block copolymers (BCPs) and guide it into nanodomains of spheres, cylinders, gyroids, or lamellae by using random copolymer brushes, surfactants, and solvent annealing [5, 6] or by the external stimuli such as heat [7-9], laser irradiation [10, 11], and UV exposure [12, 13] offers a unique opportunity to design lateral coatings with a broad range of complex patterns with periodicities ranging from a few nanometers to hundreds of nanometers can be generated using BCPs [14]. Third, importantly, polymer templates can be easily removed chemically or thermally [15-18].

The combination of these polymer properties led to the emerging material growth technique derived from atomic layer deposition (ALD) [19] called sequential infiltration synthesis (SIS). SIS is based on the infiltration of the polymer template with inorganic precursors from the vapor phase. This approach can be also called vapor phase infiltration (VPI), sequential vapor infiltration (SVI), or multiple vapor infiltration (MPI) [20]. Furthermore, the polymer template can be infiltrated with inorganic precursors from the solution [21, 22]. Subsequent removal of polymer matrix enables the full conversion of the infiltrated composite polymer structure into all-inorganic materials that replicate the structures of the original polymer hosts.

Initially, vapor-phase infiltration was utilized to improve the mechanical strength and etching resistance of the photo and e-beam lithographically prepared structures [23-29]. Infiltration of the polymer resists, for example, poly(methyl methacrylate) (PMMA), with inorganic precursors enables obtaining more precise features as a result of enhanced etch resistance of the modified polymer [30]. Later, the application of SIS was extended to BCPs [31], enabling the patterning of various materials with nanosized features [31, 32]. Also, SIS of inorganic precursors in BCP templates allowed the synthesis of inorganic and composite organic/inorganic three-dimensional periodic and random structures [20, 33].

The controlled design of patterned and nanoporous structures is critically important for a range of applications where high surface area and porosity access enable the functionality of the material systems [24, 34, 35]. Conventional methods such as optical or e-beam lithography for the nanoscale patterning are costly and time-consuming [36]. In addition to composite reinforcing [26, 37], infiltration-based synthesis, such as SIS, provides a new level of material control in terms of thickness, porosity, and composition attained upon the polymer removal [38], thus opening new application opportunities for the patterned and nanoporous structures to be used in sensing, filtering, and catalytic converting [39-41].

In this review, we will give a comprehensive summary of using the polymer templates for the design of functional materials by their infiltration with inorganic precursors from the gas phase and liquid solution. We will evaluate the range of structures and properties achievable in the SIS-synthesized materials, and review the potential use of the SIS approach for practical applications.

2. Infiltration of the polymer templates with inorganic precursors from the gas phase

SIS is based on the same sequential self-limiting chemistry as the ALD process [19, 42-44]. The combined chemo-physical nature of the SIS process includes diffusion-controlled penetration and subsequent chemisorption of inorganic precursor molecules from the gas phase inside a polymer template [38]. It integrates the ALD process for selective infiltration synthesis of inorganic material into a predefined pattern formed by the polymer [30, 45]. Traditional and the most common SIS is based on the reaction between a precursor chemisorbed inside a polymer template and water vapors [31]. However, other than water agents were utilized as well. For instance, the conversion of inorganic precursors was facilitated by exposing the materials to H_2O_2 [46-48] or O_3 [33]. **Table 1** provides the comparative overview of the ALD and SIS processes.

Table 1. *Comparison of the ALD and SIS processes for synthesis of all inorganic structures[20, 49-52].*

Process	ALD	SIS (other names - vapor phase infiltration (VPI), sequential vapor infiltration (SVI), multipulse vapor infiltration (MPI))

Substrate Requirements	None	Polar polymers or BCPs with polar domains
Typical Temperature Regime	150-200 °C	Below the glass transition of the polymers (~90-100 °C)
Cycle Duration	Short cycles: Exposure time: <1 s Holding time: 0 s Pumping time: 5 s	Long cycles: Exposure time: 1-10 s Holding time: 30-100 s Pumping time: 20-300 s
Deposition Rate	Low	High
Precursors	Volatile at the deposition temperature Highly reactive No precursor decomposition	
Precursor A	Metal halides (WF$_6$, ZrCl$_4$, TiCl$_4$, etc) Alkoxides (e.g.) Metal alkyls (e.g. TMA, DEZ, etc), β-diketonates (e.g. Y(thd)$_3$(phen), etc), organometallic cyclopentadienyl-type compounds (e.g. Cp$_2$Mg, etc) amido complexes (e.g. M(R-R'AMD)$_n$)	Metal halides (TiCl$_4$, MoCl$_5$, SnCl$_4$) Alkoxides (TIP) Metal alkyls (TMA, DEZ)
Precursor B (oxidant)	H$_2$O; H$_2$O$_2$, N$_2$O, NO$_2$ NH$_3$, PH$_3$, etc.	H$_2$O; H$_2$O$_2$, O$_3$, O$_2$ plasma, Si$_2$H$_6$
Growth Rate	1 atomic layer/cycle	40 nm – 10 μm of infiltrated BCP in 5-10 cycles.
Variations of the Process	Thermal ALD, Plasma ALD	Thermal SIS, Plasma-enhanced SIS

	Photo-assisted ALD Metal ALD Catalytic ALD	
Post-processing step	None Reductive treatment of the deposited oxidized form	Polymer removal by thermal annealing, oxygen-based reactive ion etching, or UV ozone cleaning
Structure of Materials	Amorphous, polycrystalline	Amorphous, polycrystalline
Library of Materials	A broad range of materials: Metal oxides, tellurides, fluorides, nitrides, sulfides, selenides.	Mainly oxides: Al_2O_3, TiO_2, ZnO, In_2O_3, Ga_2O_3, WO_x, VO_x, SnO_x.

As the stability of the polymers during the infiltration is critically important for predictability and consistency of the formed inorganic structures, the precursors are required to exhibit high vapor pressure at temperatures below the polymer glass transition that is typically around 100-150 ^{o}C [53]. Therefore, the majority of the initial studies on SIS focused on the synthesis of aluminum oxide (AlO_x) structures from trimethylaluminum (TMA) precursor since it has a high vapor pressure even at relatively low temperatures [54]. It is worth noting that alumina (AlO_x) formed by the reaction between TMA infiltrated into polymer containing polar functional groups and water remains the most studied SIS system [30, 31, 45, 55, 56].

2.1 The infiltration mechanism.

The SIS is based on the site-selective infiltration of the inorganic precursors into polar polymers. Dandley et al. [57] demonstrated that TMA's small size and high reactivity make it suitable for the infiltration process. Since the TMA is a strong Lewis acid [58], these reactions usually begin with the TMA forming a Lewis acid/base adduct with a strong Lewis base [59]. Poly(methyl methacrylate (PMMA) is a good candidate for the TMA infiltration because it has a large free volume and its carbonyl group is a strong Lewis base [60], which makes it favorable for the adduct formation with the TMA. Once the first adduct is formed, the TMA−PMMA reactivity

may be enhanced since the TMA is also a strong Lewis acid catalyst [61]. Notably, PMMA's reactivity is not too high to block the TMA diffusion inside the molecule.

The infiltration of the polymer template using SIS consists of the following steps: (i) Exposure of the polymer template to inorganic precursors (e.g. TMA); (ii) Removing of the inorganic precursor excess by N_2 purging; (iii) Exposure of the polymer template with incorporated inorganic precursor to water or other reacting species; and (iv) Removing of the water or other reacting species by N_2 purging (**Fig. 1a**).

The Fourier Transform Infrared Spectroscopy (FTIR) was instrumental in understanding the SIS mechanism. Since the change in wavenumber or magnitude of the FTIR peak shift is indicative of the strength of the complex formed between a functional group and the precursor, the ability of the precursor to diffuse through the polymer can be estimated by the magnitude of the peak shift. The stronger the complex, the further red the FTIR peak can be shifted [20].

Combined in situ FTIR and quartz crystal microbalance (QCM) experiments indicated that during SIS with PS-b-PMMA template, TMA readily diffuses into the PMMA and physisorbs to the ester carbonyl group (C=O) [30, 43, 45] (**Fig. 1b**). Acting as a Lewis-acid, TMA withdraws a charge from the C=O and forms a metastable $C=O\cdots Al(CH_3)_3$ that is evidenced by the shift of stretching frequency of C=O from 1732 cm^{-1} in untreated PMMA to 1670 cm^{-1} after the TMA exposure [57]. At temperature below 100 °C, C–O–Al covalent bonds do not form and TMA can easily desorb [62]. It was found that TMA exposure and purge durations have a significant effect on the AlO_x formation within the PMMA [63]. Longer TMA exposure is associated with the increase of the Al_2O_3 concentration due to the higher diffusion of the TMA molecules in the polymer template. Meanwhile, at low temperatures, as a result of the unstable nature of the PMMA-TMA complex, longer duration of the N_2 purging cycle after the TMA exposure reduces the SIS growth (**Fig. 2a**) limiting the amount of product formed after the exposure to water vapor [63].

At higher temperatures, the formation of a resonant C=O/Al-O-C complex was observed instead. The C=O/Al-O-C complex can bond itself to the substrate via a pericyclic reaction mechanism resulting in a $C-O-Al-(CH_3)_2$ group (**Fig. 1b**) [42].
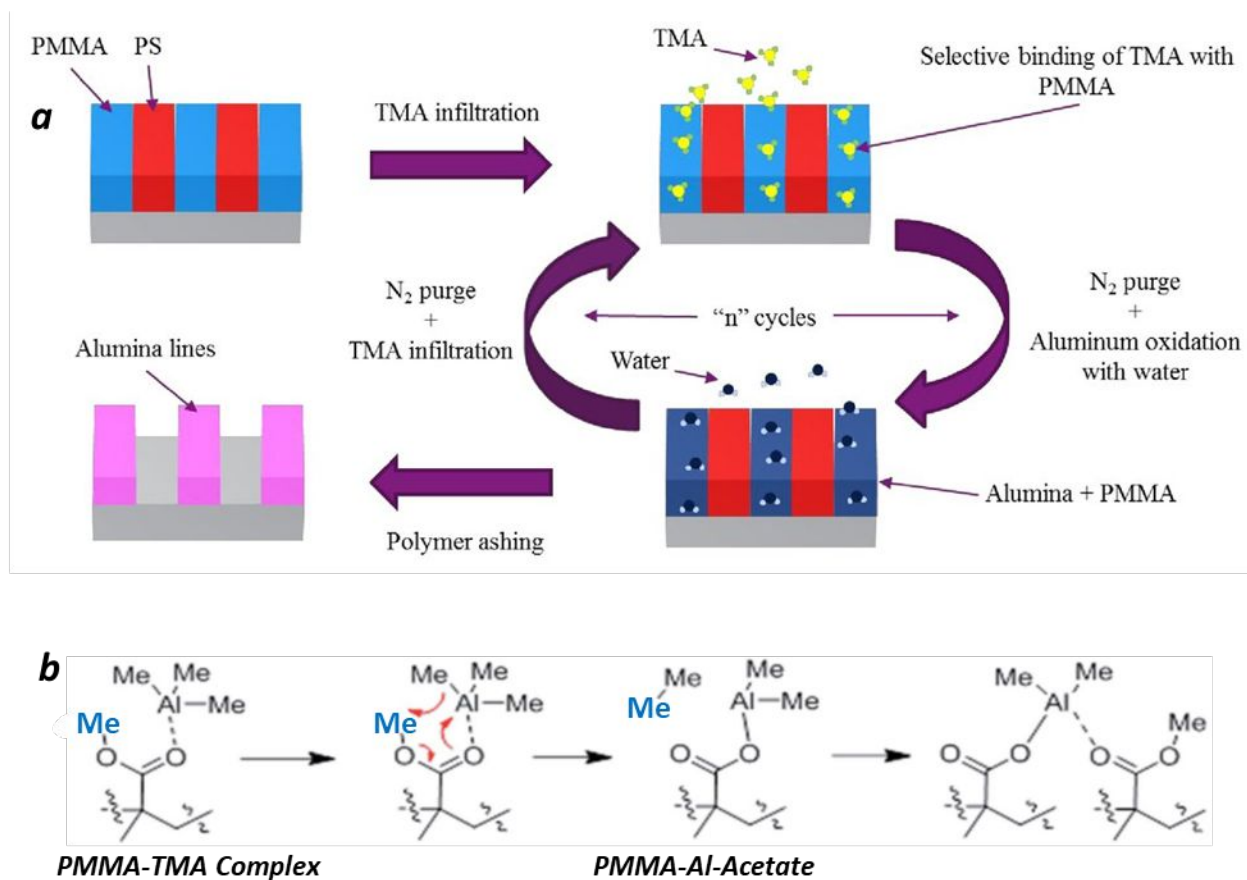
Figure 1. *(a) Schematic of the process of the vapor-phase infiltration of alumina using SIS in PS-b-PMMA polymer. Reprinted with permission from [64]. (b) Proposed mechanism of pericyclic activation of an ester-forming metal acetate from methyl trimethylacetate that is used as a model molecule for PMMA. Reprinted from [57] with the permission of the Royal Society of Chemistry.*

Dandley et al. [57] further confirmed that PMMA goes through a two-step reaction in the presence of the TMA. The first step is a fast, reversible reaction that produces a physisorbed complex. The second step is a slow, irreversible reaction of the physisorbed complex that produces a covalently bonded product structure. The authors proposed that the product formation breaks the PMMA carbonyl group to produce $O-Al-(CH_3)_2$ by a TMA methyl group [57] (**Fig. 1b**). The TMA trapped in the PMMA bulk continues to slowly react until the reaction completes. The product concentration is increased by shorter purge time and longer TMA exposure. In situ FTIR findings compared to the calculated spectra of possible product structures suggested that the second step of the reaction mechanism is a pericyclic reaction [65] that yields a covalent bond of

Al−(CH$_3$)$_2$ with O originally in the carbonyl group (**Fig. 1b**). Dandley et al. [57] found that the TMA methyl group does not shift to the carbon center but instead reacts with the PMMA methoxy group, thus producing an ester carbonyl and the ethane vapor. The second step of the reaction becomes more favorable as the temperature increases from 110 to 150°C [57].

It was demonstrated that the replacement of the H$_2$O cycle with O$_3$ as an oxygen precursor leads to the growth of alumina similar to that obtained with the standard ALD process [33]. The X-ray photoemission spectroscopy (XPS) results on alumina obtained with H$_2$O as well as with O$_3$ cycles indicate the larger amount of hydroxyl groups or water physisorbed on the surface of the alumina film after its exposure to the air. XPS results also confirm that the thermal treatment at a low temperature of alumina deposited using SIS yields the material equivalent to alumina films obtained by ALD at high temperature [33].

As the SIS process is highly selective to the polar domains, in the case of amphiphilic block copolymers, the reactions described above take place only in the domains formed by the tails of polar domains and their infiltration during a sequence of TMA-water cycles continues until the infiltration reaches saturation [45]. For example, in the case of block copolymers such as e.g. polystyrene-block-poly(methyl methacrylate) (PS-b-PMMA) infiltration occurs only within polar PMMA domains (**Fig. 1a**) [30, 31, 66]. The non-polar polystyrene part meanwhile remains unmodified [1-3]. After full infiltration, all additional TMA-water cycles result in the atomic layer deposition of aluminum oxide on top of the polymer surface [38, 67]. QCM in situ monitoring of the infiltration process allowed to evaluate the mass gain during SIS as a function of SIS cycles (**Fig. 2b**) [67]. The results indicated that the SIS procedure thus requires only 5-8 cycles for full PMMA infiltration enabling the growth of 50 nm-thick aluminum oxide, while the regular atomic layer deposition (ALD) needs about 500 cycles to grow alumina of the same thickness [68]. As a result, the SIS procedure is more time-, energy-, and cost-effective than traditional ALD [19, 68-70].
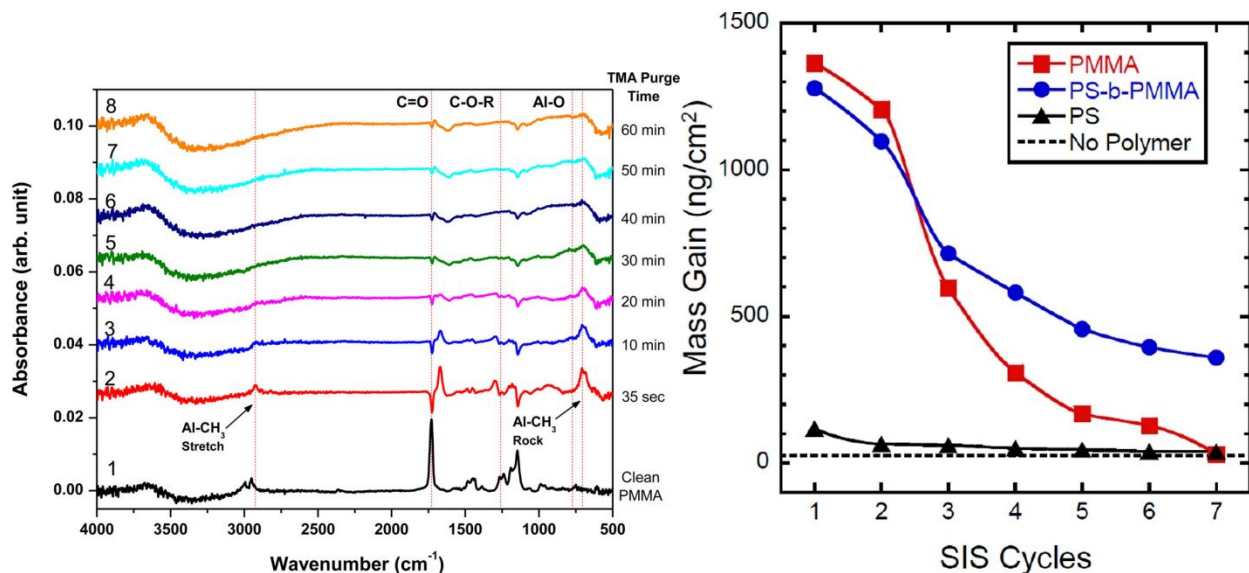
Figure 2. *Summary of the changes in the FTIR results referenced to the initial PMMA spectrum for PMMA film at 85 °C after 35 s after the first TMA dose and after different intervals of the TMA purge time (from 10 to 60 min at 10 min intervals). Reprinted with permission from [30]. Copyright (2014) American Chemical Society. (b) Mass gain measured using the QCM during the SIS infiltration of PS, PMMA, and PS-b-PMMA as a function of the cycle number. Reprinted with permission from [67].*

Dynamic spectroscopic ellipsometry (SE) based on the continuous analysis of the changes in the thickness and refractive index of the polymer template during its infiltration provided further insights into SIS kinetics [71]. In situ dynamic SE time-resolved monitoring of the polymer swelling that is indicative of the diffusion and retaining of the metal precursor in the polymer enabled the extraction of the diffusion coefficients of TMA in PMMA. The corresponding effective diffusion coefficients for PMMA films with molecular weights (M_n) such as 3.9 kg mol^{-1} and 14 kg mol^{-1} were found to be 4.5×10^{-12} cm^2 s^{-1} and 1.2×10^{-12} cm^2 s^{-1}, respectively, indicating the faster diffusion of the TMA in polymer samples with lower molecular weight [71]. The SE study also confirmed significantly larger solubility of TMA in polar PMMA than in nonpolar PS. In the case when BCPs are used as templates, the resulting metal oxide structure replicates the structure of the polar domains of the polymer template [38]. Nevertheless, Cianci et al. [71] indicated that the growth of alumina can still take place inside the PS films as a result of the diffusion of the TMA through defects in the PS film if many (more than 10) SIS cycles are performed.

Grazing incident small-angle X-ray scattering (GISAXS) technique was also utilized to further unravel the mechanism of the polymer infiltration [72]. **Fig. 3** summarizes GISAXS results on the infiltration of the polystyrene-b-poly(4-vinylpyridine) (PS-b-P4VP (75k-b-25k g/mol)) BCP with TMA and the formation of the ceramic structures during alumina SIS as a function of cycles used in the process [38]. The GISAXS patterns [72, 73] of samples prepared with three and five SIS cycles are similar. Both patterns presented a peak at $q_y = 0.0165$ Å^{-1}, which indicates 2D nanostructures laterally ordered with a d-spacing of ~38 nm. This value is consistent with the center-to-center spacing between P4VP domains in the initial BCP template [38].
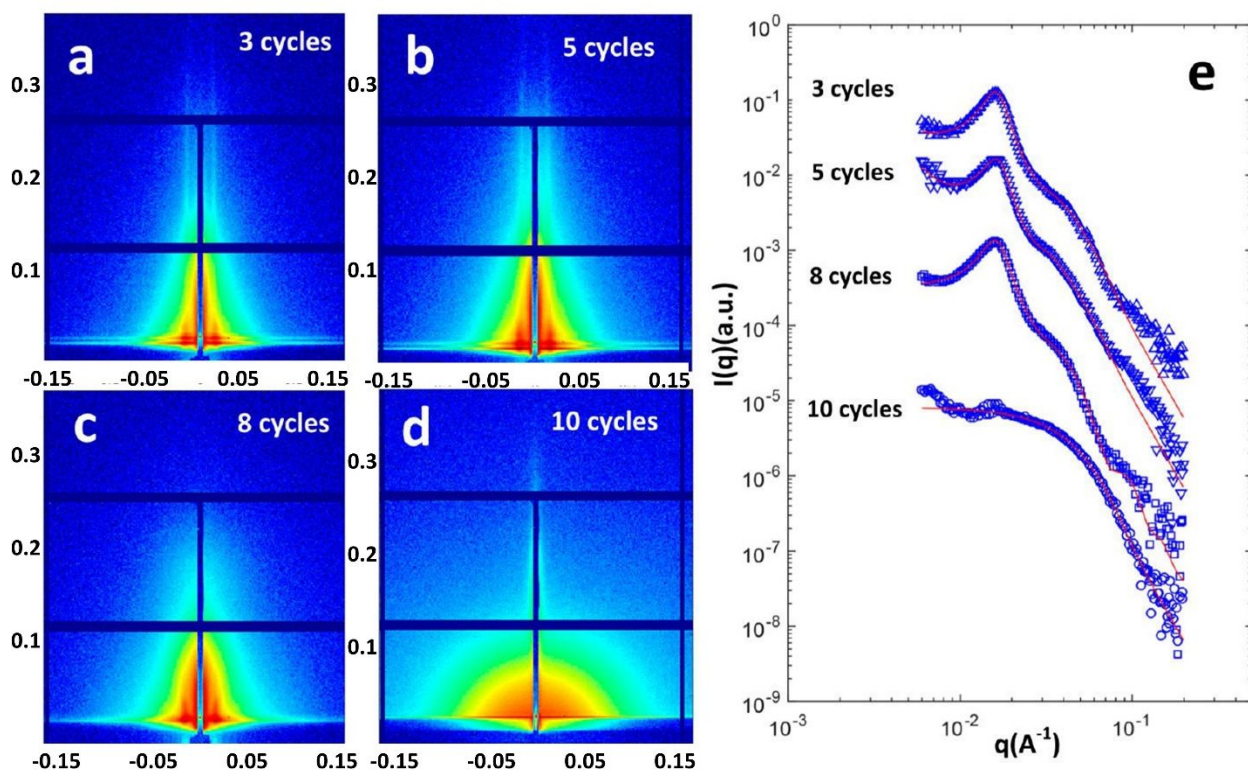
Figure 3. *GISAXS (a−d) and transmission SAXS (e) analysis of the alumina samples synthesized using the SIS process performed for a different number of infiltration cycles in the PS-b-P4VP BCP films. All the data were obtained after thermally-assisted removal of the polymer templates. In (e), the data are arbitrarily scaled for better visualization and red lines represent fitting of the data. Reprinted with permission from [38]. Copyright (2017) American Chemical Society.*

The shape of the peaks in the GISAXS spectra indicates the lateral structure is as tall as the film thickness with the peaks' weak vertical tails suggesting the coexistence of smaller features. Based on the calculations, the vertical sizes of these smaller features range from 5.0 to 6.0 nm,

slightly increasing with the number of cycles. Along the horizontal direction, there are two feature sizes, about 25 nm and 10 nm, respectively. These scattering results suggest that Al_2O_3 pillars formed with SIS are made of smaller Al_2O_3 grains. After 10 SIS Al_2O_3 cycles, the sample completely lost lateral ordering peaks; and the presence of only randomly distributed spherical 8 nm particles indicates that the Al_2O_3 particles are probably grown on the surface of the infiltrated regions of the polymer film [38].

A variety of other techniques, including in situ spectroscopic ellipsometry [74, 75], quartz crystal microgravimetry [57], quadrupole mass spectroscopy [40] and ex situ transmission electron microscope tomography [76], atomic force microscopy [77], and time-of-flight secondary ion mass spectroscopy[75] was used to follow the polymer infiltration and characterize the final inorganic structures obtained by SIS. Recently, R. Waldman et al [20] provided a very detailed overview of in situ and ex situ characterization methods of the SIS-related processes and materials [20].

2.2 The polymer templates, their tuning, and removal

A variety of metal precursors are known to infiltrate different types of polymers ranging from biopolymers (e.g. spider silk [26, 29], avian egg collage [78], polysaccharides [79], cellulose [49, 80], etc) to polymers (e.g. Kevlar [81], epoxy-based photoresist SU-8 [82], polyurethanes [40, 83], polyaniline [84], P3HT [85], PMMA [55], poly(vinylpyrrolidone), poly(acrylic acid) [42], etc). Such polymer infiltration substantially modifies their electrical, mechanical, and adsorptive properties [20].

To create patterned structures or 3D porous materials, BCPs are used. BCPs can self-assembly into periodic ordered organic materials with feature sizes ranging from ~10 to 100 nm [86-89]. In turn, the infiltration of the BCP template enables the design of inorganic patterns and porous structures [20]. Though the PS-b-PMMA remains the most common BCP template used in SIS, other BCPs such as PS-b-P4VP and block-poly(epoxyisoprene) (PS-b-PIO) copolymers are also readily accessible block copolymer templates for the direct infiltration synthesis [38, 41, 77, 90, 91]. While in the case of PMMA, as suggested from the extensive FTIR studies, infiltration with the inorganic precursors takes place at C=O and C-O-R groups of PMMA (**Fig. 2**), infiltration of the C-H groups can be observed in case of the PVP [91].

It is worth noting that the oxidative treatment of the polymer templates can alter/improve their infiltration ability. For example, UV-ozone exposure of the BCP template can increase the affinity of the inorganic precursor to the polymer via the formation of the additional oxygen-containing functional groups [92-94]. In the case of PS-PMMA, UV-ozone treatment removes ester groups from PMMA, however, creates carbonyl/carboxyl groups in PS [92]. As a result, patterns inverted from PS-b-PMMA templates can be created since the selective infiltration occurs within modified PS domains rather than within PMMA (**Fig. 4**).
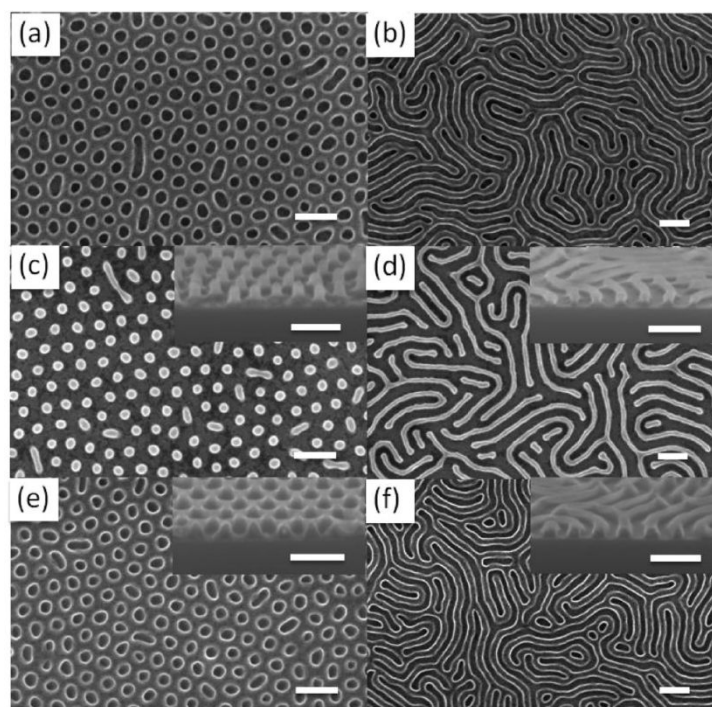
Figure 4. *SEM images demonstrating self-assembled PS-b-PMMA thin films and the corresponding Al_2O_3 nanopatterns created by selective infiltration of the polymer templates. Two cases: (a) cylindrical and (b) lamellar patterns of PS-b-PMMA films are studied. (PMMA block is removed for the SEM contrast). Images of alumina structures received (c,d) after three TMA/water cycles on unaltered (c) cylindrical- and (d) lamellar-phase templates, and (e,f) after six TMA/water atomic layer deposition cycles on UV-irradiated templates. In all images, the polymer templates were removed by oxygen plasma. Insets show the tilted cross-sectional views. Scale bars are 100 nm. Reprinted with permission from [92]. Copyright (2013) American Chemical Society.*

Due to the high reproducibility of the polymer template the resulting ceramic structure can be controlled by the original alignment of the block copolymer [77]. Specifically, if spin-coated polymers have no order, the resulting ceramic materials are very sporadic. However, the immiscibility of the polar and non-polar components leads to a spontaneous phase resulting in

mesoscopic patterns. In nonpolar solvent (e.g. toluene), the molecules of BCP form micelles with a polar part of the polymer in the center [95]. Spin-casting of the BCP solution, a traditional approach used to deposit polymer coatings, results in the formation of a pseudohexagonal array of polar domains distributed non-polar matrix (**Fig. 5**). The structure of the spin-casted BCP also depends on the solvent (**Fig. 5b**). For instance, being deposited from 1,4-dioxane PS-P4VP, polar domains orient perpendicular to the substrate, while the use of a mixture of toluene and tetrahydrofuran results in reorientation of polar cylinder domains parallel to the substrate (**Fig. 5b**). Achieving further ordering in thin BCP films requires post-deposition treatment of the films.
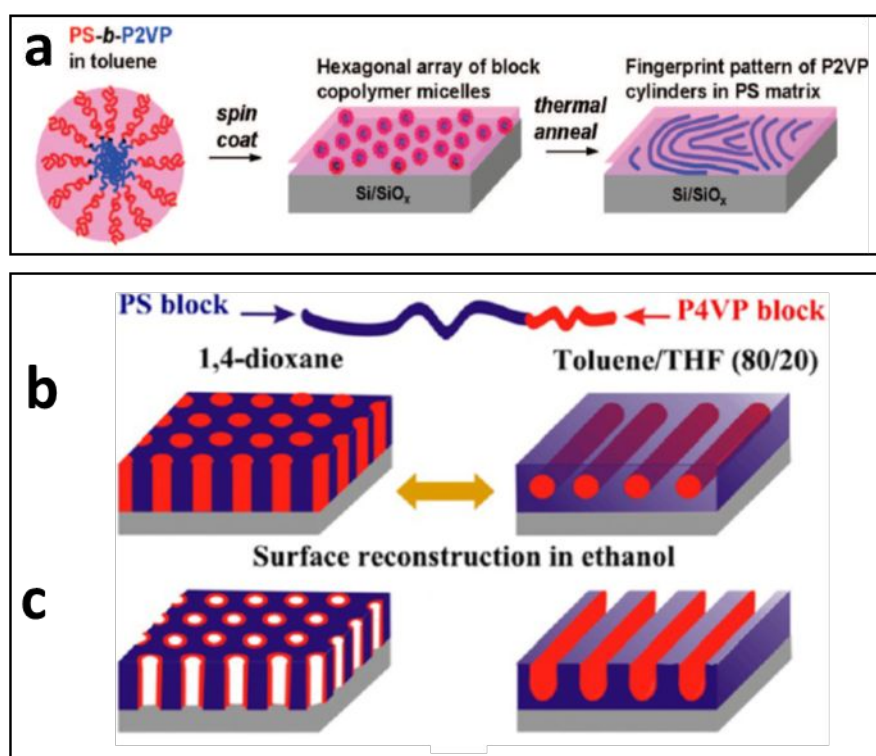
Figure 5. *(a) Pseudo hexagonal arrays are formed by spin-coating a toluene solution containing polymer micelles on a native oxide-coated silicon surface. The following thermal annealing procedure results in a fingerprint pattern of P2VP cylinders embedded within the PS matrix. Adapted with permission from [21]). (b, c) Schematics of switchable block copolymer templates during reconstruction in ethanol. Adapted with permission from [95].*

Directing the BCP structure: Thermal and solvent vapor annealing are the most common approaches to induce reorganization of polymer domains. Thermal annealing enables controlling reorientation of both blocks of the BCP by its heating above the glass transition [96] or melting temperature for some crystalline and liquid crystalline polymers [97, 98]. In the case of BCPs with

a rigid backbone (e.g. brush BCPs even with very high molecular weight), diffusion processes are fast and lateral ordering can be achieved rapidly [99]. However, in the case of BCPs with flexible backbones, diffusion is slow even at elevated temperatures due to chain entanglements that postpone the lateral ordering [99]. Solvent annealing can resolve this issue. The method is based on placing the BCP films in a solvent vapor atmosphere. The molecules of solvent penetrate the BCP film, swell it, and reduce the glass temperature transition. As a result, long-range ordering can be promptly achieved even at room temperature [100]. Coupling of solvent annealing with microwave heating further expedites the ordering of the BCP blocks. Thus, highly ordered patterns of PS-b-P2VP and PS-b-PMMA polymer families were obtained in less than 3 min [101].

In the case of the PS-b-PMMA template, both thermal and solvent treatments of the PS-b-PMMA template [22, 102] can be used to enable different nanopatterns of AlO_x including vertical lamella, vertical cylinders, and inverse cylinders (holes) as well as three-dimensional multilayered heterostructures [22, 102]. The polymer domain readjustment by controlling parameters of deposition and annealing [12, 103-105] successfully modifies the resulting ceramic film [31, 38]. In the previous studies, it was shown both horizontal and vertical alignment of the ceramic structures produced with SIS (**Fig. 6**) [31].
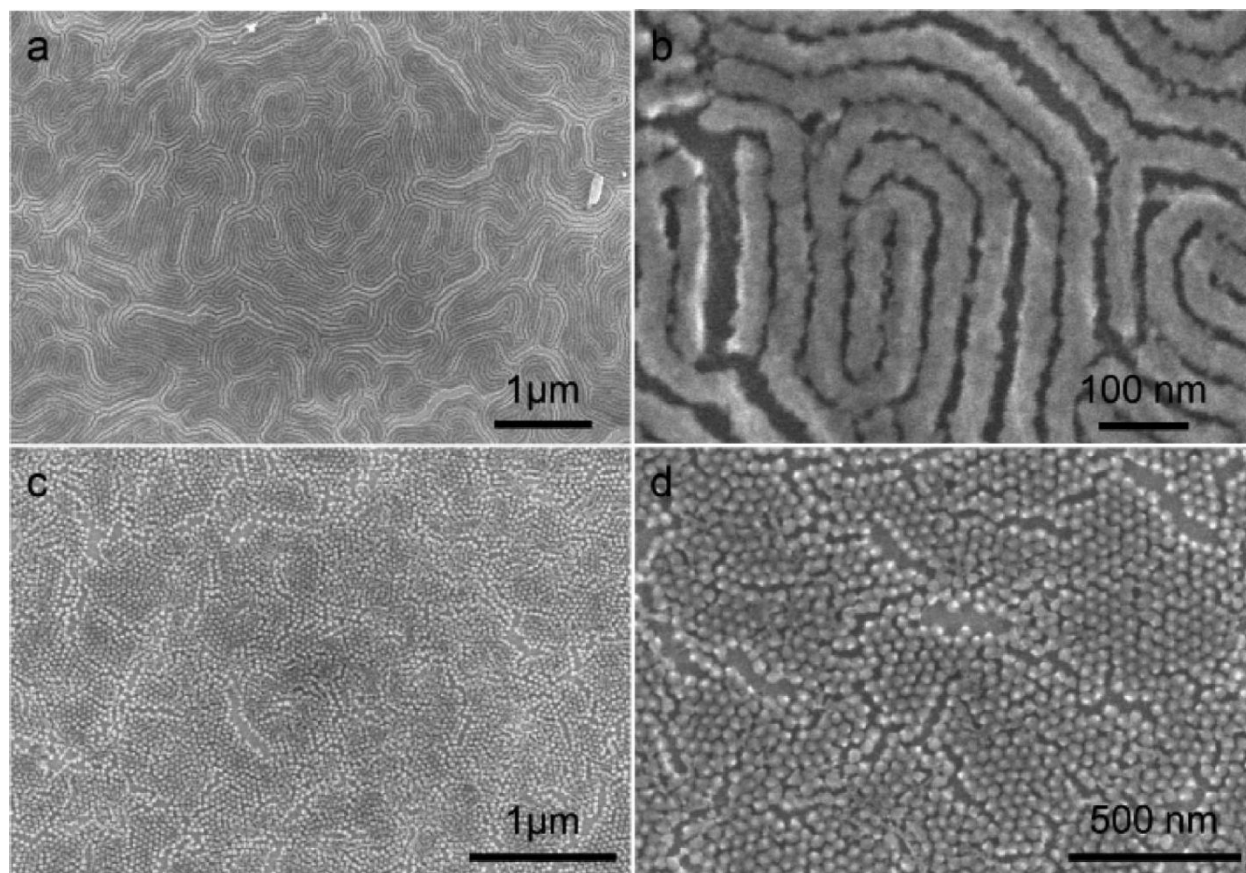
Figure 6. *Field emission SEM (FESEM) micrographs of SiO$_2$ (a, b) nanocylinder patterns and (c, d) nanopost patterns on Si wafer formed after one cycle of sequential exposure to TMA and silanol vapors followed by heating at 400 °C for 12 hours. Reprinted with permission from [31]. Copyright (2011) American Chemical Society.*

Thermal or solvent annealing, though, are the processes that do not allow active control over the density of the structural defects and ordering direction. Different modifications of the annealing such as thermal zone heating [106] and photothermal approach [107] were proposed to expedite the ordering kinetics in BCPs as well as direct the ordering. Majewski et al [107] demonstrated that photothermal gradients generated by localized laser heating could increase the ordering kinetics of BCP thin films by at least three orders of magnitude compared to conventional oven annealing [107]. A sweeping laser front allows guiding the thermal gradient and, hence, direct the ordering of the BCP (**Fig. 7a**). This photothermal technique called laser zone annealing (LZA) enables the rapid alignment [108] of BCPs over macroscopic areas (**Fig. 7b**). However, LZA requires the substrates coated with the layer that generates heat upon light adsorption (e.g., Ge) (**Fig. 7a**).
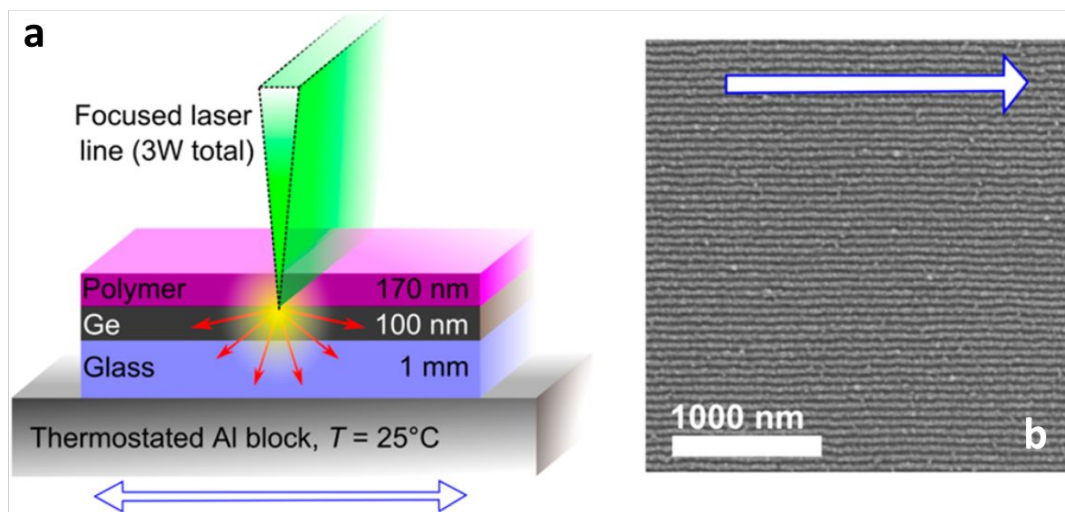
Figure 7. *(a) Schematic of the laser zone annealing (LZA) technique: a polymer sample with Ge layer underneath mounted on a motorized stage; the layer of Ge absorbs the light and induces heating thus resulting in the patterning of a polymer. (b) SEM image of the patterned polymer film. Adapted with permission from [107].*

Modification of the BCP template by swelling: While the structure of the deposited BCP film can be efficiently tuned by thermal and solvent annealing, the major limitation of SIS is slow diffusion of the TMA precursor vapor through the free volume of the polymer, once the top layer (40-50 nm) is fully infiltrated [31, 66, 109]. As a result, SIS was used mainly for the deposition of thin, less than 50 nm in thickness, structures. The swelling of the BCP template before SIS was proposed to increase the infiltration depth [38].

The swelling of the polymers modifies them by incorporating the organic solvent into the polymer matrix [110, 111]. When the polymer consists of two different domains, as in the case of block copolymers, swelling is an effective technique for introducing additional polymer porosity, enabling an easier infiltration process. **Fig. 8** shows that swelling of the PS-b-P4VP polymer in ethanol, which is selective to swelling of the P4VP part only, for 1 h at 75°C before infiltration leads to the formation of a thick porous Al_2O_3 SIS film with random structure [38].
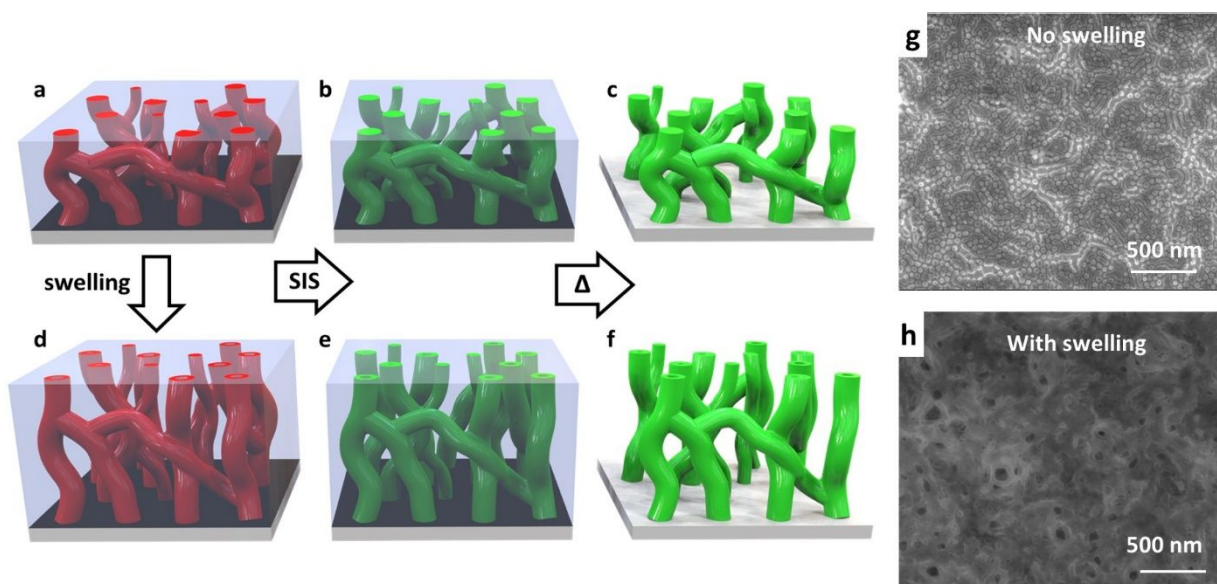
Figure 8. *Increased thickness of the nanoporous alumina in comparison to (a-c) regular SIS process is possible via (d-f) swelling of the PS-b-P4VP polymer in ethanol, which creates additional channels for effective infiltration of the TMA inside the polymer film. Red is the polar domain of the polymer, green is resulting alumina oxide infiltrating only polar part, gray is non-polar polymer removed after SIS. The SEM micrographs present the resulting alumina structures received (g) without and (h) with swelling. Adapted with permission from [38]. Copyright (2017) American Chemical Society.*

The evolution of the structures during swelling and infiltration was further evaluated with combined uses of QCM, atomic force microscopy (AFM), and scanning electron microscopy (SEM) analysis [77]. Thus, swelling of 110 nm thick PS-b-P4VP BCP (75k-b-25k molecular weight) film in ethanol at 75°C in ethanol enabled access to all available polar domains of the BCP and resulted in two times larger alumina mass absorption and four times larger effective pore volume formation than the ones in case of non-swollen polymer (**Fig. 9**) [77].
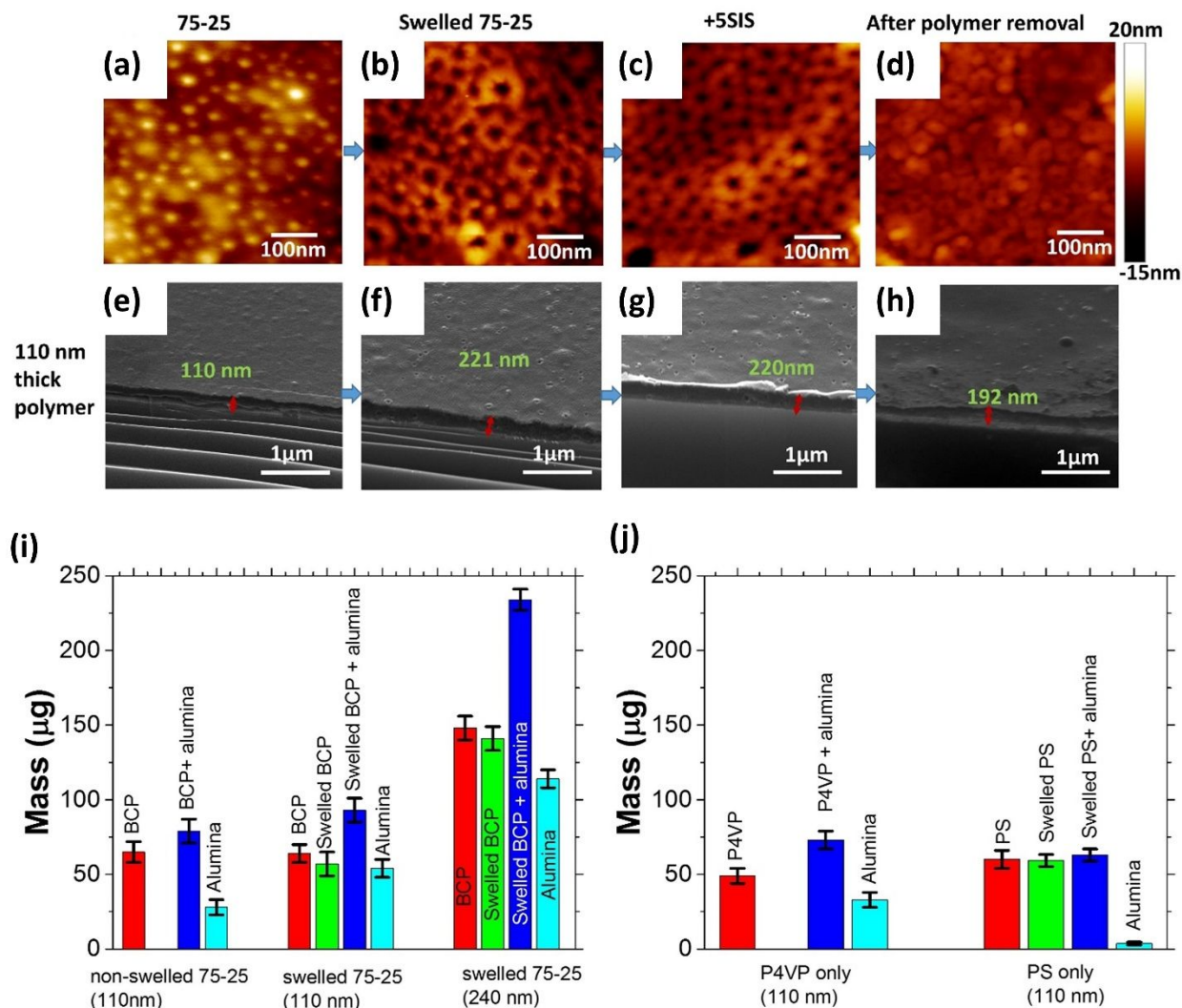
Figure 9. *(a-d) AFM height profile images and (e-h) the corresponding SEM cross-section analysis performed at a tilted angle for PS_{75k}-b-$P4VP_{25k}$ BCP films (110 nm thick) during different stages of swelling and infiltration. Mass gains during swelling and infiltration of (i) PS_{75k}-b-$P4VP_{25k}$ BCP films and (j) monopolymers are analyzed using the QCM. Adapted with permission from [77]. Copyright (2019) American Chemical Society.*

It is also worth noting that being supersaturated blends of BCP and additives (e.g. polystyrene-*block*-polyethylene oxide (PS-*b*-PEO) and a PEO oligomer) can separate into an additive-rich and a BCP phases where one block of BCP gets selectively swollen by the additive [112]. The supersaturation can be induced by the control over temperature or through quick solvent evaporation. Rinsing out both phases with the solvent that dissolves additive leads to the hierarchical pore formation (**Fig. 10**) [86]. This process was called spinodal-decomposition–

induced macro- and mesophase separation plus extraction by rinsing or SIM^{2}PLE [112]. This post-deposition approach was reported to result in the fabrication of structure with a continuous interface between meso- and macro-porous regions [86]. In addition to SIM^{2}PLE, non-swelling induced phase separation (SNIPS) was proposed to form hierarchically porous films that can be used as separation membranes. SNIPS is based on the plunging of the polymer into precipitation (non-solvent) bath (**Fig.10**) [86].

Though both approaches for creating porous polymer structures were not yet utilized in the SIS process, they seem to be promising for the efficient design of highly porous 3D structures suitable for a broad range of applications.
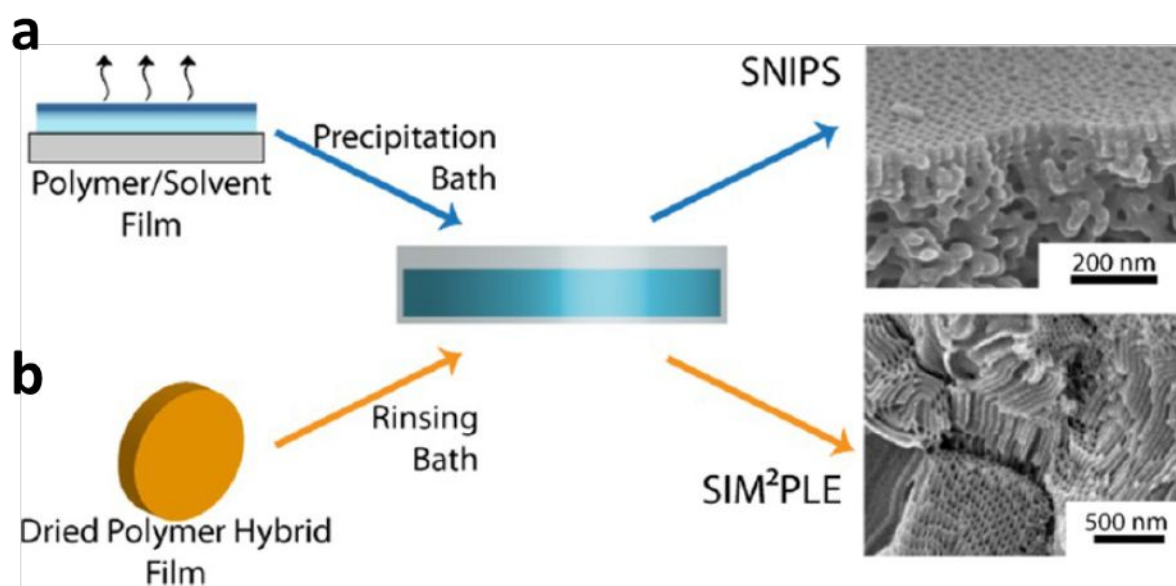
Figure 10. *Depiction of the SNIP (a) and SIM^{2}PLE (b) approaches. In SNIP BCP dissolved organic solvents are deposited on the substrate and partially dried and plunged into a non-solvent bath. The organic solvent in the film exchanges rapidly with the non-solvent thereby freezing the film structure into the solid-state of the BCP. In SIM^{2}PLE the solution of BCP and additive (e.g., oligomer) is dried and placed in the rinsing bath with selective solvent for additive. Reprinted with permission from [86].*

Removal of the polymer template: After the template infiltration, the resulting materials are organic-inorganic hybrids. The conversion of the polymer infiltrated with inorganic precursors into all-inorganic material is achieved by a post-processing procedure, including thermal annealing

in an oxygen environment, reactive ion etching, or exposure to ultraviolet ozone cleaning [38]. Thermal annealing or calcination of materials in a flow of oxygen or air, in addition to the polymer removal, allows reconstruction and densification of the porous structures providing their better mechanical stability [38]. The annealing procedure can be further optimized by changing the maximum heating temperature and time of the annealing. It should be noted, however, that thermal annealing may result in some pore shrinkage and be incompatible with many temperature-sensitive substrates, such as, for example, single crystal quartz used as a substrate for sensing platforms [41].

An alternative method involves UV ozone cleaning [113, 114] as a slower process allowing to prevent substrate damage. However, the process may lead to the trapping of the residual carbon in the cavities of the inorganic structure. Therefore, very prolonged exposure to the cleaning procedure is needed [39]. Interestingly, alumina that is obtained using both UV ozone cleaning and thermal annealing processes is highly amorphous [115].

2.3 3D Porous Structures Created by SIS and Accessibility of the Pores

The introduction of the swelling step allowed to expand the SIS applicability from thin films to the highly porous bulk structures [38] and thus to broaden its use to different areas, in which materials are immersed or in contact with liquid media. High accessibility of the pores for liquid penetration and efficient mass flow is, therefore, critically important characteristics of the SIS-designed materials [24, 34]. She et al. [41] demonstrated that the nanoporous alumina synthesized via SIS is highly hydrophilic and enables access of water inside the available pore volume (**Fig. 11**). Specifically, using the QCM technique, highly sensitive to the surface structure and surface interactions with surrounding media [116-119], it was shown that the resulting nanoporous alumina structures, when immersed in water or acetone, tend to absorb up to 95% of liquid [41]. To probe the interconnectivity of these pores, the surface access of the liquid was blocked by the deposition of graphene layers. 20% of uncovered alumina, however, still allowed to fill up to 60 % of the available porosity volume [41]. Summary of the porosity access to water and acetone is included in Table 2.
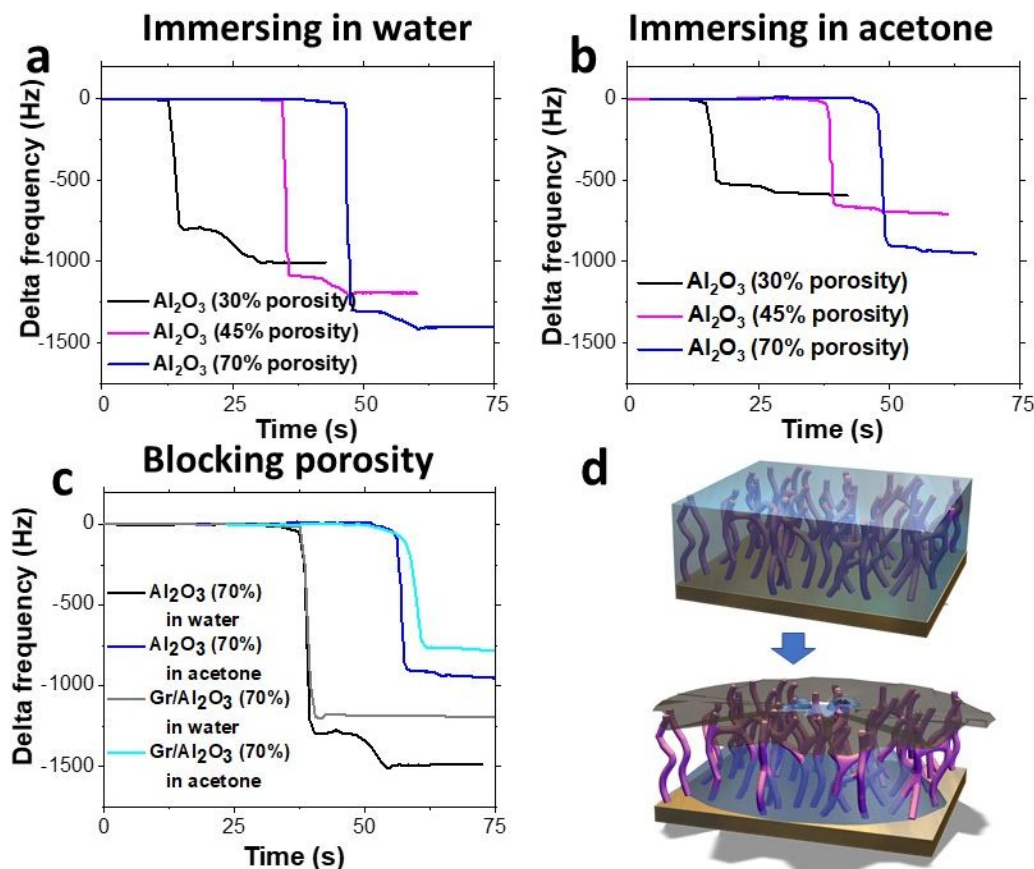
Figure 11. *Changes in the resonant frequency of the oscillations of the QCMs with alumina films of different porosity grown using PS-b-P4VP polymer templates with varying relative concentrations of polar/non-polar domains upon (a) immersing in water and (b) acetone. (c) Blocking of the surface access to the alumina (with initial 70% porosity) pores using transferred graphene films indicates a high interconnectivity of the pores. (d) Schematics of the pores blocking. Adapted with permission from [41].*

Table 2. *The frequency shift values and estimates for the effective volume of pores filled with water and acetone upon immersion [41].*

Sample	Viscosity effect (Hz)	Liquid in pores effect (Hz)	Effective volume of pores with solvent (%)
Al_2O_3 (70%) in water	-715	-780	98%
Al_2O_3 (70%) in acetone	-360	-580	94%
Al_2O_3 (45%) in water	-715	-479	93%
Al_2O_3 (45%) in acetone	-360	-336	84%
Al_2O_3 (30%) in water	-715	-292	85%
Al_2O_3 (30%) in acetone	-360	-220	83%

2.4 The structures and heterostructures obtained by SIS - beyond alumina.

Precursors beyond TMA used for the synthesis of AlO_x are often characterized by slower diffusion and, subsequently, lower sorption of vapor-phase precursors has been reported [120]. Nevertheless, a plethora of metal oxide structures such as SiO_x, TiO_x, VO_x, WO_x, SnO_x, ZnO, GaO_x, InO_x, etc was synthesized using the SIS process. For this, the TMA precursor was replaced with tris(tertpentoxy)silanol [31], titanium tetrachloride or titanium tetraisopropoxide [90], vanadium oxytriisopropoxide [90], tetrakis(dimethylamino)tin(IV) [46], diethyl zinc [121], trimethylindium [55], trimethylgallium [55], etc. The efficiency of the infiltration of the inorganic precursor is affected by the nature of a metal precursor. For example, trimethylindium and trimethylgallium can similar to TMA reversibly interact with C=O groups of PMMA, however with a significantly lower affinity that results in their rapid diffusion within the polymer film [55]. As a result, the rapid growth of Ga_2O_3 and In_2O_3 takes place. The growth of In_2O_3 was observed already at 80 ^{o}C that is well below the onset temperature of the ALD using the same precursors [55].

However, in the majority of other cases, organometallic precursors and polymer moieties interact weakly, and hence, the first AlOx SIS cycle generating the priming layer of alumina is needed to promote the additional metal oxide growth within the polymer [122]. It is worth noting that the deposition of ZnO requires priming of the polymer with TMA during the first cycle when PS-PMMA or PS-PVP templates are used [22] since direct infiltration of diethyl zinc followed by polymer removal results in the formation of only sparse zinc oxide nanoparticles [90, 92]. However, the use of PS-b-PIO copolymer templates enables the successful infiltration of diethyl zinc without priming [90]. **Fig. 12** shows the effect of the polymer template on its infiltration with the inorganic precursors.
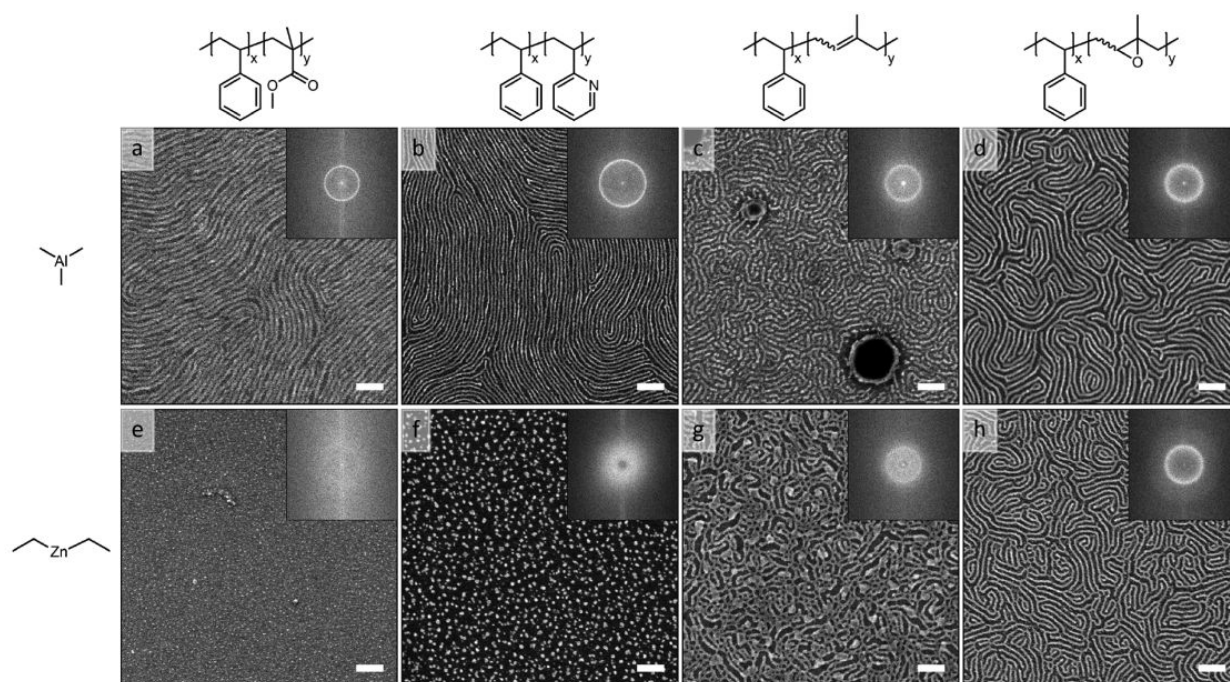
Figure 12. *SEM micrographs highlighting the effect of the polymer template on its infiltration with the inorganic precursors. Different (a−d) AlO_x and (e−h) ZnO patterns synthesized by SIS followed by O_2 plasma removal of the BCP templates: (a, e) PS_{46}-b-$PMMA_{21}$, (b, f) PS_{33}-b-$P2VP_{12}$, (c, g) PS_{32}-b-PI_{12}, and (d, h) PS_{29}-b-$PI_{13}O100$. Insets included in each micrograph show the 2D fast Fourier transformed spectra. Scale bars are 200 nm. Reprinted with permission from [90]. Copyright (2019) American Chemical Society.*

Recently Segal-Peretz et al. [122] demonstrated that SIS could be used for heterostructure array fabrication. The synthesis is based on sequential exposure of the BCP film to two organometallic precursors. First, BCP is shortly exposed to the first precursor; however, the time of the exposure is adjusted in a way to limit its penetration to the upper part of the film only, while the second precursor consequently diffuses deeper into the film. BCP template removal results in a metal oxide heterostructure array (**Fig. 13**).
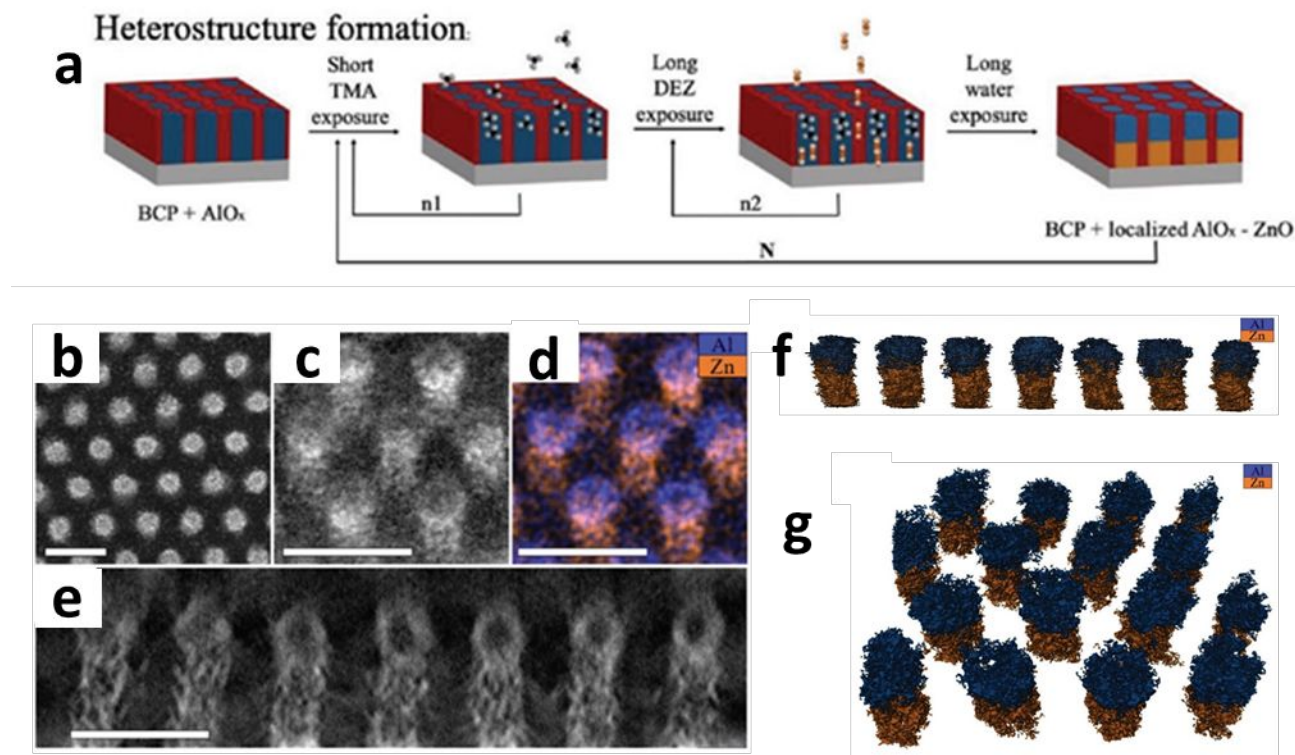
Figure 13. *(a) Schematic of the process of the heterostructure array fabrication. Characterization of aluminum oxide/zinc oxide nanorods prepared by spatially-controlled SIS using PS-b-PMMA BCP: high-angle annular dark-field scanning transmission electron microscopy (STEM) images taken at (b) 0° tilt, and (c) 10° tilt, and (d) corresponding energy-dispersive x-ray spectroscopy (EDS) map taken at 10° tilt; (e) cross-sectional image of nanorods. Reconstruction images of (f) cross-sectional view, and (g) perspective view of the STEM-EDS tomography. Scale bars in the images are 50 nm. Adapted with permission from [122]. Copyright 2019. Wiley-VCH.*

2.5 Water SIS vs Plasma SIS.

As we mentioned above, traditional SIS is based on the reaction between a precursor chemisorbed inside a polymer template and water vapors [31]. However, elevated temperatures required for this reaction in the thermal SIS are incompatible with moisture sensitive and thermally unstable surfaces or interfaces. Previously, plasma-enhanced ALD (PEALD) [123] demonstrated advantages over thermal ALD such as higher quality of the deposited materials, lower impurity content and better electronic properties; lower deposition temperature; increased choice of precursors and materials; tuned stoichiometry of the compositions as a result of deposition under nonequilibrium conditions and increased growth rate [124]. It is worth noting that SIS can be realized via plasma-enhanced conversion of a metal precursor [91]. For instance, exposure of

TMA molecules to oxygen plasma also leads to the synthesis of conformal alumina coating with controlled thickness and porosity [91]. Moreover, an oxygen plasma step of the process facilitates the production of fully infiltrated nanoporous structures within one cycle, as compared with a minimum of eight cycles required in water-based thermal SIS [38], hence minimizing the time of the synthesis of highly porous structures [91].

When plasma-enhanced SIS (PE SIS) is performed on the PMMA polymer, the changes in the FTIR spectrum (**Fig. 14**) of the PMMA polymer upon exposure to PE SIS procedure indicate the stretching in carbonyl C=O (at $\sim$ 1729 cm^{-1}), ester C-O-R (at $\sim$ 1145 cm^{-1} and $\sim$ 1260 cm^{-1}), and C-H (at $\sim$ 2950 cm^{-1}) as well as bending of C-H (at $\sim$ 1450 cm^{-1}) bonds [125, 126]. The observed peaks are similar to the thermal SIS process. Exposure of the polymer to plasma only (in the absence of inorganic precursors) for the same amount of time is not associated with any observable changes in the absorbance, thus confirming the absence of damage to the polymers during plasma exposure [91]. Therefore, the PE SIS can be used as an alternative to the thermal SIS infiltration process, compatible with materials sensitive to water vapors but not damaged by the exposure to oxygen plasma.
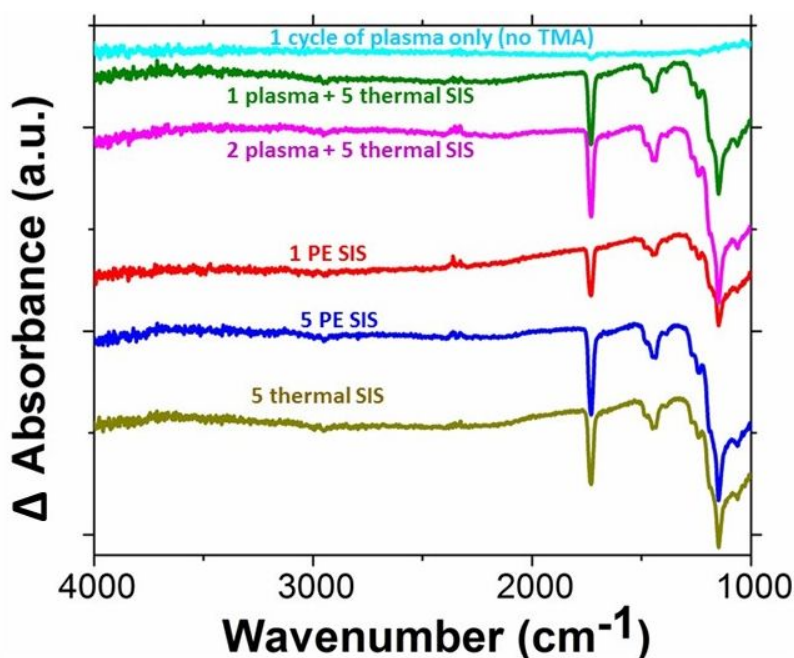
Figure 14. *FTIR delta absorbance measurements for the PMMA film after thermal and plasma-enhanced SIS processes referenced to the initial PMMA. Reprinted with permission from [91]. Copyright (2017) American Chemical Society.*

2.6. Shortcomings of the polymer-template infiltrated synthesis

Although the SIS offers unique opportunities for fabrication of conformal and 3D porous structures, there is a number of limitations associated with the nature of the polymer template. In contrast to the traditional ALD process that enables uniform growth of conformal coatings, the polymer-template infiltration highly depends on the quality and uniformity of the polymer templates. As a result, defects in the polymer films largely affect the SIS-designed materials. SIS process is also limited by the infiltration dynamics of the polymer template. As a result the thickness of the resulting structures is controlled by the diffusion of the inorganic vapors. To increase the infiltration depth, additional porosity can be introduced by swelling, though the resulting highly porous structures can become mechanically unstable and may experience shrinkage during the polymer removal process. Alternatively to swelling, the polymers with the lower molecular weights can be considered [71], though there is still the thickness limit defined by the diffusion efficiency.

Glass transition of the polymer at temperatures above 100 °C as well as polymer melting at elevated temperatures narrowing the range of the precursors that can be used for deposition of different structures thus limiting the compositional diversity of the synthetized structures. At the same time, exposure of the polymer template to oxidants as a requirement of the SIS process can result in the template alteration that, in turn, can lead to a significant deviation of the deposited structure from the polymer templates.

3. Infiltration of the polymer templates with inorganic precursors from the solution

One major limitation of the SIS processes, both water-based thermal SIS and plasma-assisted SIS, is the need for high vapor pressure precursors, which are often associated with high-temperature processing conditions incompatible with a low glass transition temperature of the polymers. In contrast to the limited availability of materials for vapor-phase infiltration, the liquid phase infiltration approach provides more flexibility in terms of material selection. The traditional approach uses inorganic precursors electrostatically coordinated into micelle cores in forms of cations, as neutral salts or as metals in acidic presursors [127]. Block copolymer templates can be

used for the synthesis of uniformly sized nanoparticles (NPs) homogeneously dispersed within the polar domains. Polar domains in BCP can be loaded with the metal precursors from the solution by simple immersion of the polymer in an aqueous metal salt solution [21, 128]. Subsequent reduction of adsorbed metal ions or complexes by exposure to hydrogen at elevated temperatures or by immersion in an aqueous sodium borohydride results in the formation of metal nanoparticles [128]. J. Chai et al [21] demonstrated that metal ion loading of the P2VP block with aqueous solutions of anionic metal complexes is accomplished via protonation of this basic block [21]. As a result, due to electrostatic interactions, protonated P2VP domains accumulate high local concentrations of metal precursors [21]. A subsequent brief plasma treatment removes the polymer and produces inorganic nanostructures with shape replicating the shape of the polar domains in the deposited BCP [21] (**Fig. 15**). Using infiltration of the PS-P4VP thin film deposited on a Si substrate with $PtCl_4^{2-}$ precursors, Chai et al [21] fabricated the arrays of horizontal Pt nanowires. Majewski et al. [22] converted meshes formed by PS-b-P2VP cylindrical patterns using metal salts complexation of the P2VP blocks into meshes of metal nanowires with all possible two-dimensional Bravais lattices (**Fig. 16**) [22].

Figure 15. *(a) Schematic of the polymer-based patterning approach for different metals on a silicon substrate. SEM images of synthesized structures with varying composition: (a) Au, obtained from HAuCl₄/0.9% HCl(aq); (b) Pd, obtained from Na₂[PdCl₄]/0.9% HCl(aq); (c) Fe, obtained from K₃Fe(CN)₆/0.9% HCl(aq); (d) Co, obtained from K₃Co(CN)₆/0.9% HCl(aq); (e) Cu, obtained from CuCl₂/0.9% HF(aq); and (f) Ni, obtained from NiCl₂/0.9% HF(g) [21]. Adapted with permission from [21].*
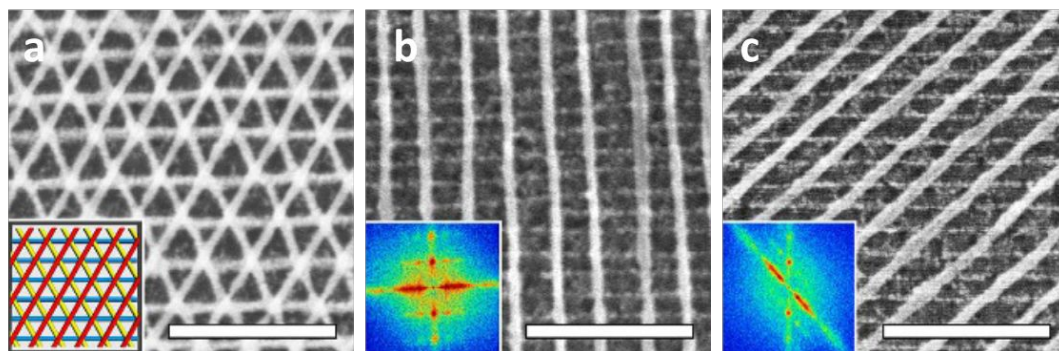
Figure 16. *Platinum nanostructures fabricated using a soft-shear laser zone annealing (SS-LZA). SEM images and corresponding Fourier transform of (a) a Pt triangular mesh; (b) Rectangular Pt lattice; and (c) Oblique lattice. Scale bars are 200 nm. Reprinted with permission from [22].*

In addition to aqueous solutions, the infiltration of inorganic materials in polymer templates can be achieved using the swelling of the polymers. For this, in a prior study, the metal precursor powders in the form of a metal acetylacetonate were dispersed in ethanol which is selective to polar domains of the PS-b-P4VP BCP template [39]. Using this approach of liquid phase infiltration during the swelling of PS-b-P4VP polymers followed by SIS, synthesis of palladium oxide, ruthenium oxide, cobalt oxide, etc. in nanoporous alumina was demonstrated [39]. Relative loading of metal oxides and aluminum oxide materials can be controlled by the adjustment of the concentration of acetylacetonate in ethanol. After the infiltration with both materials, the removal of the BCP template using thermally-assisted burning in an oxygen atmosphere at 450 °C results in the formation of NPs (4.3 ± 0.2 nm) of palladium oxide uniformly distributed in the alumina matrix (**Fig. 17**) [39].
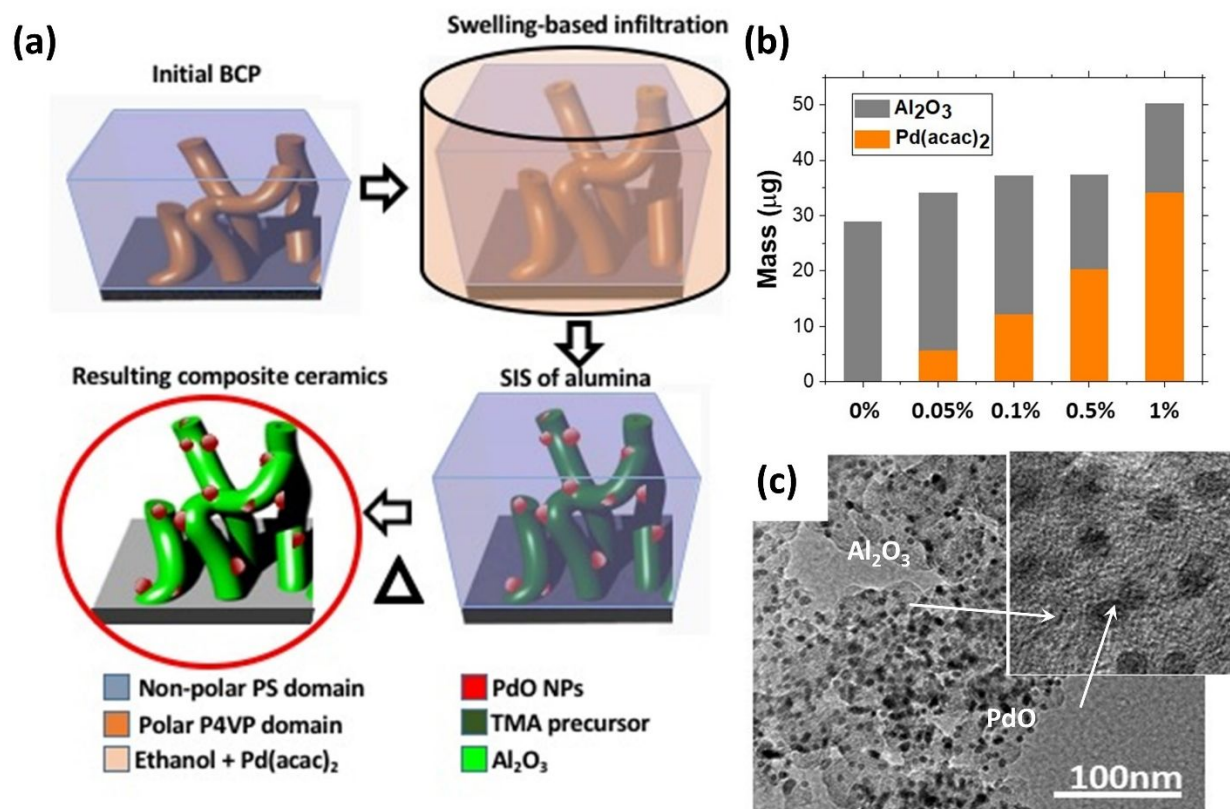
Figure 17. *(a) Schematic of the deposition process highlighting different stages of two-step infiltration: initial BCP is immersed in ethanol with dissolved* Pd(acac)$_2$ *powder at 75°C for 1 hour; the dried sample is infiltrated using the SIS process; the final sample is burned to remove the polymer template. (b) QCM analysis summarizing the mass change during SBI absorption of Pd(acac)$_2$ and SIS absorption of alumina as a function of Pd(acac)$_2$ concentration in ethanol. (c) TEM images of the resulting PdO NPs in alumina structure. Adapted with permission from [39].*

4. Applications of the infiltration-designed materials

The previous sections highlight the major mechanism of the polymer infiltration approach and the properties of the materials designed with it. Simplicity and universality of the infiltration approach sparked an interest in using it for a wide range of applications [85, 129-132]. The deposited patterned polymer films can further serve as chemically-resistant etching masks enabling precise texturing of the surfaces [12, 104, 133]. Additionally, such precise control over surface morphology enables the fabrication of hydrophobic [35, 134, 135] and hydrophilic [136] coatings, with their interactions with liquids being controlled by the periodicity of the structures

antireflective materials with refractive index controlled by porosity [38], sensing systems with large surface area access [137], etc. In the following sections, we summarize the recent progress on using polymer template infiltration with inorganic precursors for the design of functional coatings and nanoporous materials.

4.1 Design of oleophilic polymers

Modification of the polymer by the SIS process enabled the design of oil adsorption foams, oleo sponge [40]. Infiltration of alumina in highly porous polyurethane created a substrate for oleophilic silane-based compounds, (3aminopropyl)triethoxysilane and butyldimethyl(dimethylamino) silane, prominent to binding with oil molecules [138]. Once the sponge is inserted into an oil spill, the high reactivity of the oleophilic molecules leads to the adsorption of the oil [40]. The oil is further released from the sponge and the sponge is reused for adsorbing additional oil spills. **Fig. 18** summarizes the improved adsorption capacity of the SIS modified oleo sponge when immersed in different oils. In comparison with the untreated polyurethane foam, the crude oil sorption capacity for functionalized polyurethane foam improved from ~7g per gram to 30 g per gram of the foam material [40].
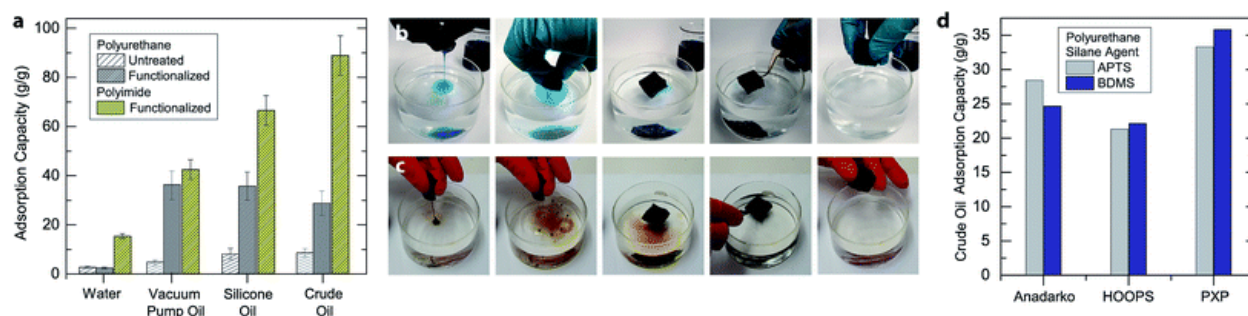
Figure 18. *(a) Sorption capacities of untreated and SIS/silane functionalized polyurethane foams as well as of an SIS/silane functionalized polyimide foam. Photographs of the sorption/compression cycle of the (b) dyed silicone oil and (c) crude oil removal process from a water bath. (d) Crude oil sorption properties are shown for two oleophilic silane agents, such as g-aminopropyl triethoxysilane (APTS) and butyldimethyl(dimethylamino)silane (BDMS). Reprinted from [40] with the permission of the Royal Society of Chemistry.*

4.2 Antireflective coatings

In another study, SIS was successfully implemented for the design of graded refractive index antireflective coatings [38]. In contrast to widely-used conventional single-layer ARCs that target only a particular wavelength at normal incidence [139-142], minimization of the reflection over a broad spectrum is possible by implementing graded-index coatings with omnidirectional broadband properties [139]. Porosity introduction via creation of voids with refractive index equal to 1 allows significant reduction of the refractive index of the bulk materials [143-145] and thus controlling the optical properties of materials. To achieve the graded porosity, the alumina films were grown by the sequential infiltration synthesis in polymers of varying composition and thickness [38]. Ellipsometry analysis confirmed that refractive indices of the SIS-designed alumina coatings measured at a wavelength of 785 nm are inversely proportional to their porosity, varying from 1.2 at 60% porosity to 1.39 at 25% porosity. Thus, porosity enabled a substantial reduction of the refractive index of alumina in comparison to characteristic bulk alumina (1.8) and amorphous ALD Al_2O_3 (1.6) [146]. Using the SIS approach, two types of coatings were designed: the single-layer antireflective coating minimizing the green light reflection (**Figs. 19a and 19b**) and multi-layer gradient porosity antireflective coating minimizing light reflection in a wide range (**Figs. 19c and 19d**) [38]. In the case of the multi-layer coating, the thin uniform porosity layers were synthesized one-by-one (by a sequence of spin-coating of the polymer, infiltration, and burning-assisted polymer removal steps) and multi-stacked on top of each other. The reflection of light in a broad spectrum range from the multi-layer coating on the glass substrate substantially reduced from 4% to 0.1%, while transmission increased from 92% to 95% (**Fig. 19**).
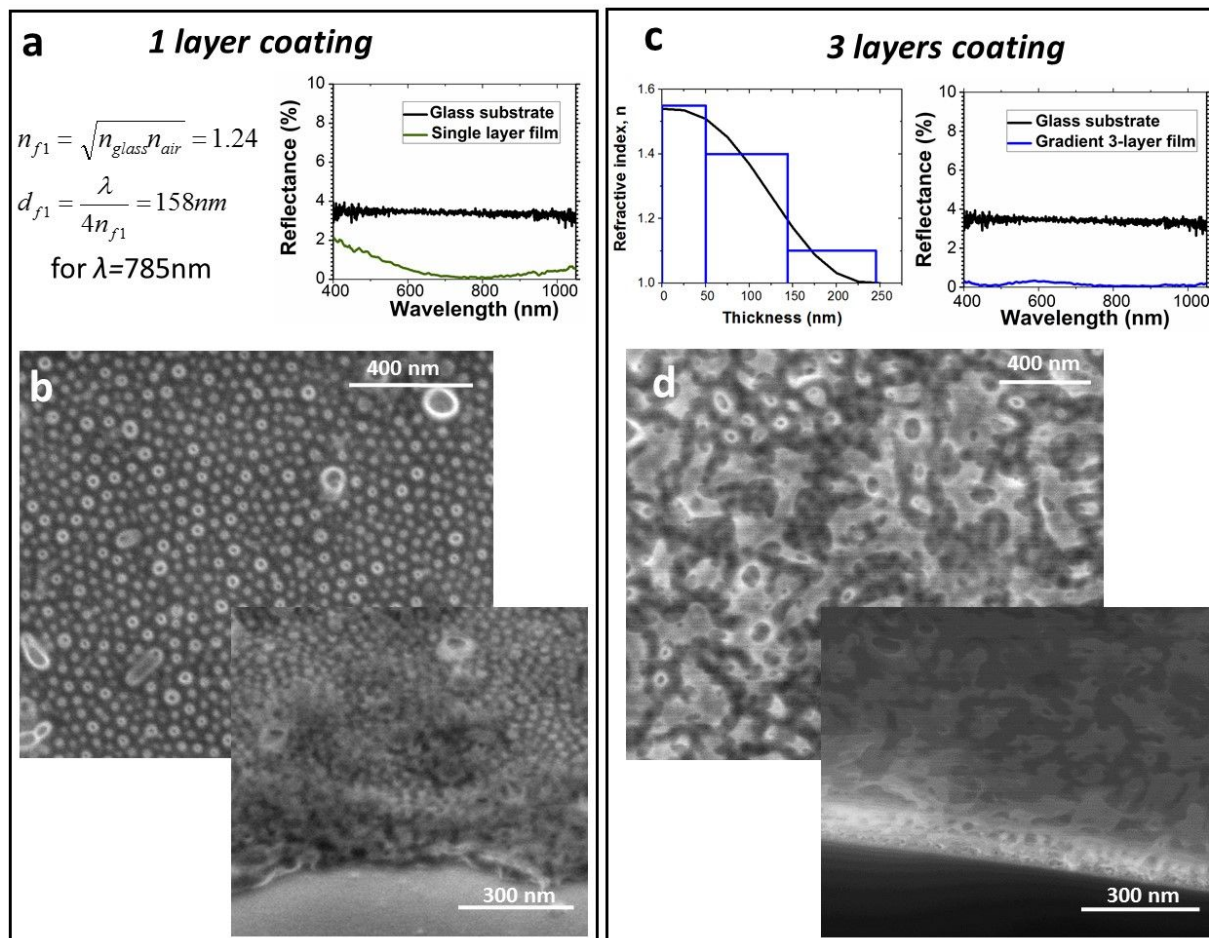
Figure 19. *Two cases of antireflective coatings with single wavelength minimized reflection for 785 nm light (a,b) and a wide range minimized reflection for a range of 400-1050 nm (c,d). Reflectance measurements and corresponding SEM micrographs of porous (a) and (b) 1-layer and (c) and (d) 3-layer Al_2O_3 coatings on silicon substrate fabricated by the swelling-assisted SIS process. Reprinted with permission from [38]. Copyright (2017) American Chemical Society.*

4.3 SIS-enhanced lithographic patterning

While thin carbon-based polymer films are rather poor etch masks, since they gradually degrade during plasma etching, infiltration of the polymers that are traditionally used as photoresists in the photo and e-beam lithography with inorganic materials improves their etch resistance. For example, etch resistance of PMMA and ZEP520A (a copolymer of chloromethacrylate and methyl styrene) can be improved by factors of 37 and 5, respectively, without degradation of the line-edge roughness of the patterned features [23]. As a result, a transfer

of sub-100 nm deep patterns became possible with the implementation of the SIS thus eliminating the need for an intermediate hard mask (**Fig. 20**).
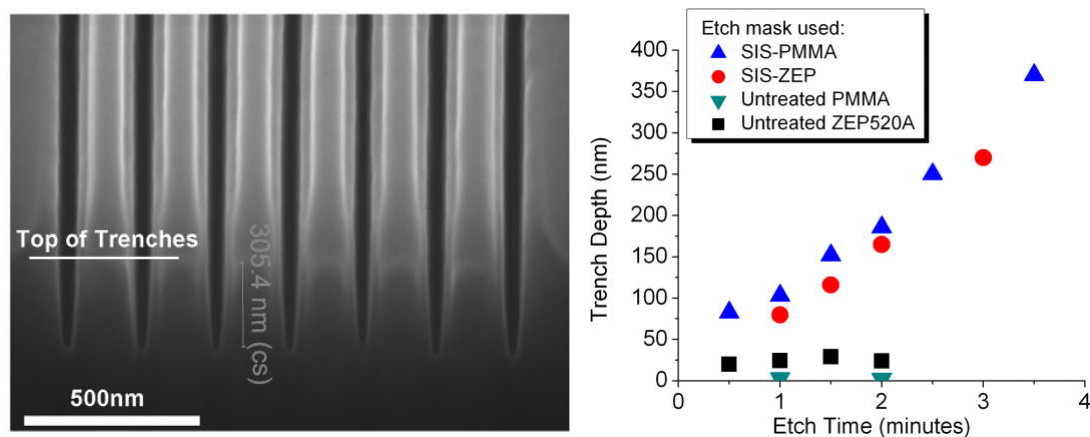
Figure 20. *SIS-PMMA assisted lithographic patterning of (a) 50 nm wide, high aspect-ratio trenches directly etched in Si. (b) Corresponding trench depth in silicon as a function of etching time for untreated and SIS-treated masks. Reprinted with permission from [23].*

Ruiz et al. [147] demonstrated that directed BCP assembly opens up a possibility to multiply and improve lithography enabling obtaining smaller features and denser patterns. A combination of this approach with SIS enables the direct patterning of the surface with ceramic structures.[148] Suh et al. [133] further implemented high etch resistant SIS generated patterns for sub-10-nm lithographic patterning of the silicon wafer. Specifically, with the use of an etch-resistant initiated chemical vapor deposited (iCVD) polymer topcoat layer, the authors succeeded in assembling the grating structures in the P2VP-b-PS-b-P2VP block copolymer. The aligned structures were further immobilized by exposing the polymer to cycles of the TMA and water vapors infiltrating the polar domains. After polymer removal in oxygen plasma, the resulting alumina pattern was used for reactive ion etching (RIE)-based selective etching of silicon. As a result, the lithography approach became more robust and compatible with a wide range of processing requirements, such as for example high temperature up to melting point of alumina at 2000 °C, limitations for which previously arose from the polymer instability under temperature and gas exposure. Recently, directed self-assembly of the BCP combined with self-aligned double patterning followed by SIS allowed reaching 10.5 nm full pitch [149]. Starting with patterns with 84 nm pitch lines formed by e-beam a total pitch scaling factor of 8 was demonstrated that is a step forward to addressing the challenge of fabricating bit-patterned media with bit densities beyond 5 Tb/in^2 that corresponds to

an 11 nm bit period. Such densities in the patterned structures are required for emergent heated-dot mangetic recording technology that enables increasing bit density keeping high signal-to-noise ratio and good thermal stability [149].

4.4 Triboelectric nanogenerators

With the recent interest in designing more efficient energy systems, polymer infiltration offers a direct approach to the synthesis of functional composite structures. In a study by Yu et al. [56], alumina infiltration was used for improving power efficiency in triboelectric nanogenerators [56]. By doping the triboelectric polymers with alumina via SIS, the authors enabled better durability and higher power density of the produced triboelectric nanogenerators (TENG). The designed polydimethylsiloxane (PDMS)-based triboelectric nanogenerator showed ten times increase in the charge transfer amount upon alumina doping [56]. Such an improvement is attributed to the difference in electron affinity of PDMS film and alumina-doped PDMS film [150]. Similar results were demonstrated for Kapton and PMMA films, highlighting the successful infiltration of alumina molecules into the polymer films for tuning their electrical properties [56]. While a traditional approach for TENG design implies the use of different polymers, the SIS process enables the design of high-performance TENG devices with the same polymer materials (**Fig. 21**).
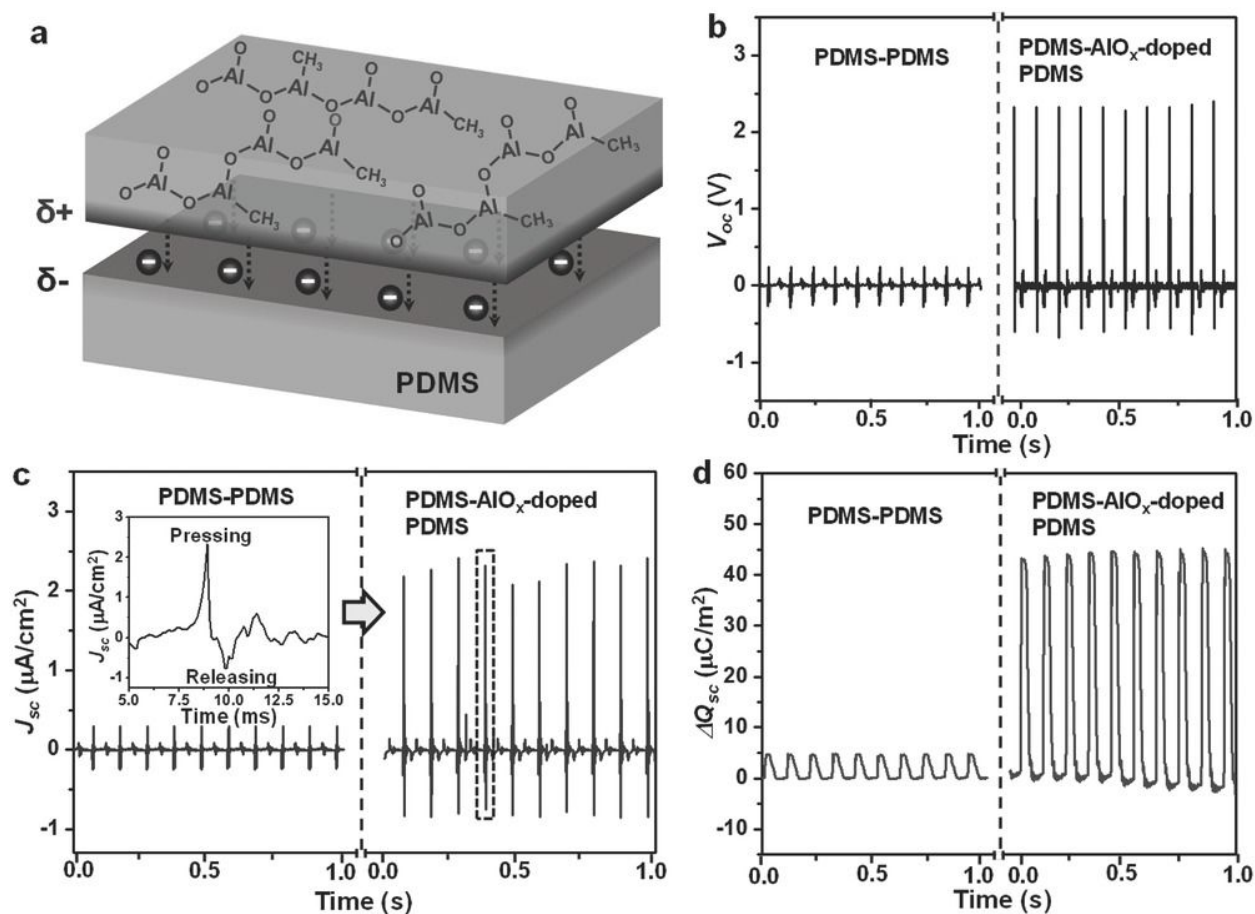
Figure 21. *Enhancing the design and performance of PDMS triboelectric nanogenerator (TENG) using SIS-based alumina doping: a) Schematic of the charge distribution between pristine PDMS and alumina-doped PDMS films upon cycling of the TENG. Comparison of b) the open-circuit voltage (V_{oc}), c) short-circuit current density (J_{sc}) and d) charge transfer amount characteristics of PDMS and PDMS-alumina TENGs. Adapted with permission from Ref. [56]. Copyright 2015. Wiley-VCH.*

4.5 Sensing of gases and water vapors

Metal oxides are extensively used in the detection of gases with their sensing ability being strongly related to surface reactions [151]. For instance, the working principle of chemoresistive gas sensors is based on the change in the conductivity of the metal oxides upon the interaction of their surface with the gas molecules [152, 153]. Since SIS is the most suited for the synthesis of metal oxides lateral coatings and it is compatible with lithography, it naturally provides an exciting

opportunity to access new forms/structures of metal oxides for sensing. However, there are only a few examples of the utilization of SIS-based synthesis in material fabrication for sensing [137]. The relative novelty of SIS can be one of the reasons. Another reason can relate to the fact that direct SIS enables coatings fabrication with the thickness limited by the penetration of the inorganic precursors inside the polymer and hence only thin coatings (less than 50 nm) could be obtained. However, the progress in the thickness control, for example, by swelling or utilization of different types of polymer templates is likely to facilitate the application of SIS for the synthesis of metal oxides for sensing. Below we provide a few examples demonstrating the applicability of the SIS for the synthesis of materials relevant for sensing.

Recently, L. Ocola et al [137] demonstrated that the infiltration of the epoxy-based negative photoresist SU-8 with ZnO enabled the synthesis of the sensors for highly sensitive detection of gases such as formaldehyde and NO_2 with better than 5 ppm sensitivity [137]. SU-8 allowed deeper penetration (~500 nm) of the inorganic precursors. It is worth noting that the polymer template was not removed and the final composite material was utilized for sensing.

In addition to this, alumina is widely recognized as a promising material for monitoring humidity changes [154-156]. Since the surface of alumina prepared via SIS is highly porous and hydrophilic [41], and water rapidly infiltrates its pores, SIS-designed nanoporous alumina films were tested for their ability to sense humidity at atmospheric pressure and room temperature [41]. For this, alumina was deposited on the QCM surface in the form of a 200 nm thick nanoporous (~70% porosity) film. **Fig. 22** summarizes QCM resonant frequency change when the system is inserted into a vacuum chamber and humidity is introduced gradually in the form of water vapor [41]. Adsorption of water vapors on the surface of the nanoporous structure of the QCM results in a significant change in resonant frequency response when exposed to low relative humidity values; in contrast, solid alumina films obtained by 200 ALD cycles does not respond to small humidity variation [41]. A similar contrast difference between bulk and porous structures has already been explored by Lazarovich et al. [156]. 13 μm thick nanoporous alumina films produced by anodizing the bulk QCM electrode material were used to sense the presence of the water vapors [156]. SIS-designed alumina, though, demonstrates much higher sensitivity, attributed to the interconnectivity of the pores in SIS-produced alumina films (**Fig. 22**).
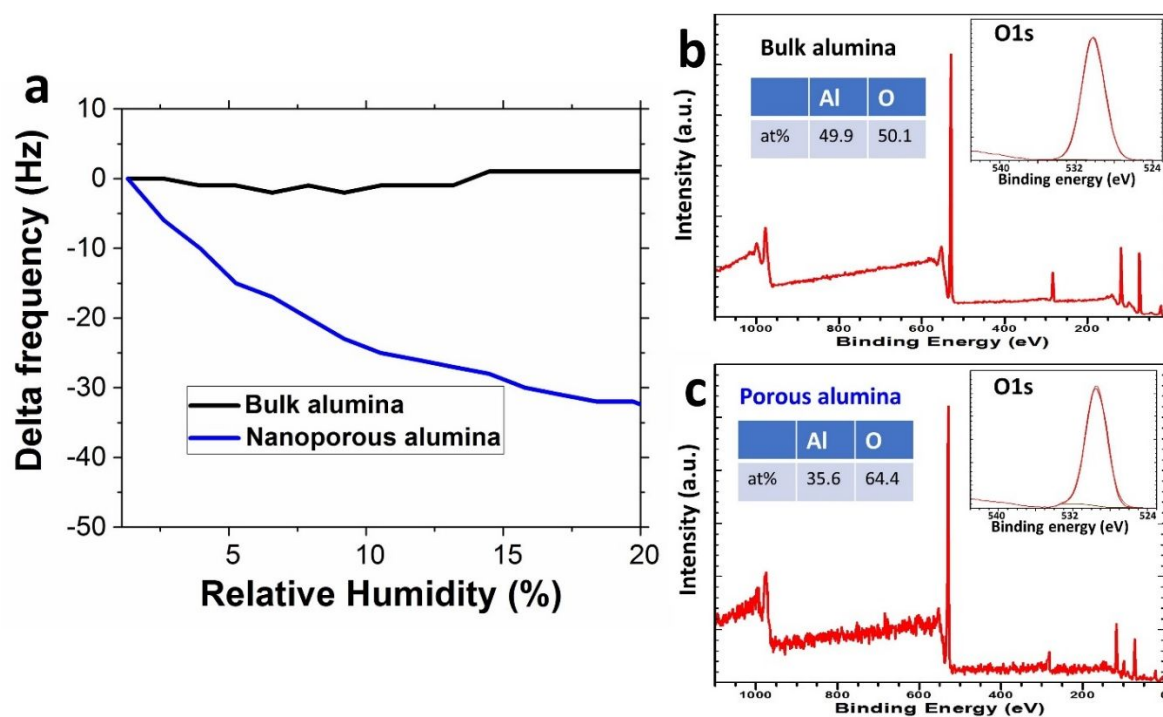
Figure 22. *Humidity sensing using QCM with SIS-deposited highly porous alumina on the QCM surface. (a) Changes in the delta frequency of the QCM oscillations as a function of relative humidity for the QCMs coated with bulk alumina and SIS-based nanoporous alumina demonstrating much higher sensitivity of SIS-designed nanoporous alumina in a lower humidity regime. Corresponding x-ray photoemission spectroscopy (XPS) analysis of the (b) bulk and (c) porous alumina confirms the higher presence of oxygen groups in porous alumina. Adapted with permission from [41].*

4.6 Catalytic materials

The development of highly reactive catalysts for the conversion of combustion reaction gasses has remained an active research area for decades [157]. Catalytic converters substantially reduce hazardous gas emission from combustion engines [158, 159]. Supported palladium catalysts exhibit great durability and excellent activity related to the presence of a palladium oxide phase [160, 161], though they suffer from sintering under elevated temperature conditions.

In recent studies, the polymer infiltration process has been employed for the synthesis of palladium nanoparticles directly in the nanoporous alumina matrix (**Fig. 17**) [39]. To control the selectivity of the infiltration sites and to differentiate between and among the infiltrated materials, the SIS approach was combined with the swelling based infiltration process. Palladium centers were created by infiltrating the block copolymer infiltration during the swelling step; for this, the

metal precursor in form of palladium acetylacetonate was dissolved in ethanol that is the selective swelling agent for polyvinyl pyridine domain of the PS-b-P4VP block copolymer [110]. Five cycles of the SIS process followed by thermally-assisted removal of the polymer template at 450 °C resulted in the formation of 4.3 ± 0.2 nm palladium nanoparticles embedded in the alumina matrix [39]. The resulting PdO in alumina samples were tested as catalysts for carbon monoxide oxidation and methane combustion reactions. These catalytic tests confirmed accessibility of PdO NPs embedded in the alumina matrix to the reactive gases and demonstrated high temperature stability of the materials thus indicating the great application potential of the infiltration approach to be used for the design of catalytic materials (**Fig. 23**). In the case of the CO oxidation, both the samples without pre-treatment and the samples after pre-treatment demonstrated similar temperatures for complete oxidation. These results are in agreement with previously reported data for traditional alumina-supported palladium particles [162]. Similarly, in case of the methane combustion, pre-treatment of the samples showed no effect on the methane conversion temperature at ~550 °C confirming high stability of the designed materials [39].
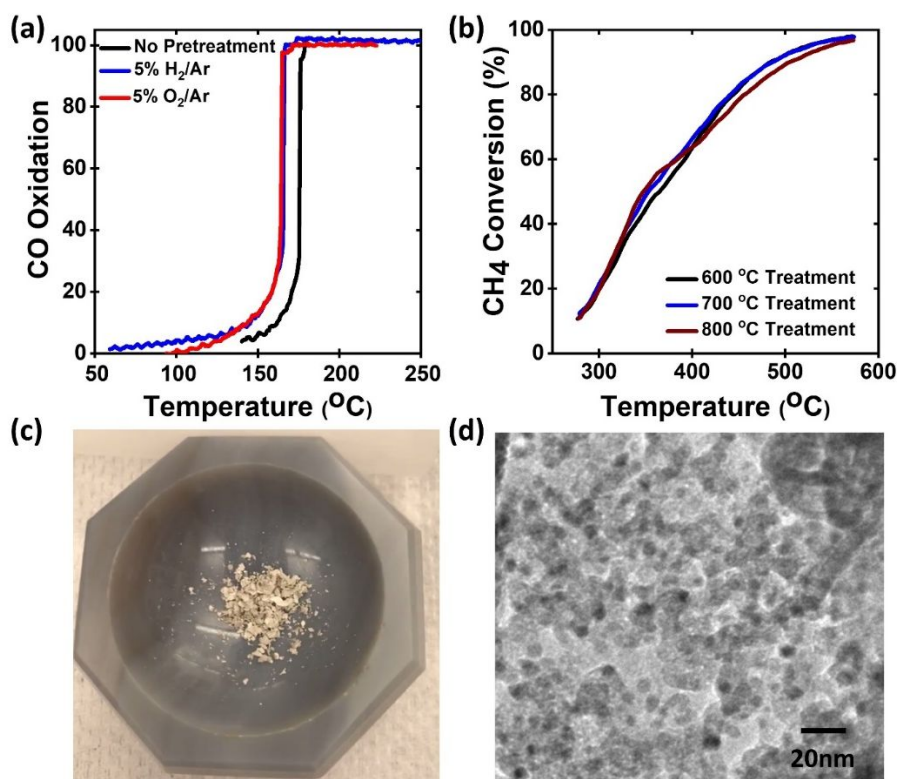
Figure 23. *The catalytic activity of the samples with ~10 wt% of PdO NPs in alumina toward (a) CO oxidation and (b) methane conversion. (c) Photograph of the sample and (d) corresponding*

transmission electron microscopy image of the sample after the high-temperature catalytic activity tests. Adapted with permission from [39]. Copyright (2019) American Chemical Society.

Conclusions

The polymer template infiltration approach is a powerful platform toward a synthesis of an unlimited library of materials. This review highlights the recent progress in developing the sequential infiltration synthesis approach for the design of nanoporous ceramics with different porosity, structure, and composition. In particular, the dynamics of the infiltration process and the effects of the parameters on the resulting structure of the materials are covered. Further, recent progress on using the infiltration synthesis for specific applications is presented. These dedicated studies have confirmed the following key findings.

- The polymer template infiltration process allows the low-temperature synthesis of nanoporous ceramics of a wide range of compositions.
- The selectivity of the infiltration process is defined by the contrast of polar/nonpolar domains in the polymer precursor.
- The swelling of the polymer can be used for increasing the vapor infiltration depth and for further tuning of the structure of the material.
- The nanoporous ceramics demonstrate high interconnectivity of the pores accessible to different solvents.
- Polymer template infiltration enables defined-by-the-polymer template precise control of the structure while substantially increasing the thermal, mechanical, and chemical stability and reliability of the functional components.

It is worth noting that despite a relative novelty of a polymer-based infiltration approach, it demonstrated exciting opportunities to design surfaces, modify and create materials of practical importance. However, it did not reach its full potential. Further development of this synthetic platform is likely to be associated with the utilization of different types of polymers and their treatments. Currently, AB-type of BCPs, where A and B are polar and non-polar chains, respectively, is commonly used as a polymer template to create patterned or 3D porous structures. More complex polymer structures such as triblock, multi-block, bottle-brush BCPs as well as block

copolyelectrolytes where one block has charge groups along the backbone[163] can enable the access to more diverse morphologies of the polymer templates [164, 165].

Bridging polymer science and material science communities will expedite the progress in the synthesis of functional hybrid and all-inorganic materials with unique special and compositional features. For instance, the use of an ABC type of BCPs with tailored functional groups for selective infiltration can be instrumental to the direct synthesis of multicomponent heterostructures. Also, substantial progress in the synthesis of the heterostructures can be achieved by combining the infiltration of metal precursors from the solution and gas phases. Additional studies on the effect of the molecular weigth of polymer and diffusion of the precursor molecules [71] are needed. The utilization of the plasma ALD in infiltration processes is also likely to extend the compositional diversity of the structures synthetized by polymer infiltration approaches.

Acknowledgments

References

[1] Y. Xie, D. Kocaefe, C. Chen, Y. Kocaefe, Review of research on template methods in preparation of nanomaterials, Journal of Nanomaterials 2016 (2016) 11.

[2] X. Zhao, L. Lv, B. Pan, W. Zhang, S. Zhang, Q. Zhang, Polymer-supported nanocomposites for environmental application: a review, Chem. Eng. J. 170 (2011) 381-394.

[3] W. Gacitua, A. Ballerini, J. Zhang, Polymer nanocomposites: synthetic and natural fillers a review, Maderas. Ciencia y tecnología 7 (2005) 159-178.

[4] K.J. Van Bommel, A. Friggeri, S. Shinkai, Organic templates for the generation of inorganic materials, Angew. Chem. Int. Ed. 42 (2003) 980-999.

[5] J. Oh, H.S. Suh, Y. Ko, Y. Nah, J.-C. Lee, B. Yeom, K. Char, C.A. Ross, J.G. Son, Universal perpendicular orientation of block copolymer microdomains using a filtered plasma, Nature Communications 10 (2019) 2912.

[6] K.W. Gotrik, C. Ross, Solvothermal annealing of block copolymer thin films, Nano Lett. 13 (2013) 5117-5122.

[7] R.A. Segalman, H. Yokoyama, E.J. Kramer, Graphoepitaxy of spherical domain block copolymer films, Adv. Mater. 13 (2001) 1152-1155.

[8] M.P. Stoykovich, M. Müller, S.O. Kim, H.H. Solak, E.W. Edwards, J.J. De Pablo, P.F. Nealey, Directed assembly of block copolymer blends into nonregular device-oriented structures, Science 308 (2005) 1442-1446.

[9] J.Y. Cheng, A.M. Mayes, C.A. Ross, Nanostructure engineering by templated self-assembly of block copolymers, Nature Materials 3 (2004) 823-828.

[10] H.M. Jin, S.H. Lee, J.Y. Kim, S.-W. Son, B.H. Kim, H.K. Lee, J.H. Mun, S.K. Cha, J.S. Kim, P.F. Nealey, K.J. Lee, S.O. Kim, Laser Writing Block Copolymer Self-Assembly on Graphene Light-Absorbing Layer, ACS Nano 10 (2016) 3435-3442.

[11] A.G. Jacobs, C. Liedel, C.K. Ober, M.O. Thompson, Understanding of PS-b-PMMA phase segregation under laser-induced millisecond thermal annealing, Alternative Lithographic Technologies VII, International Society for Optics and Photonics, 2015, pp. 942309.

[12] J. Bang, U. Jeong, D.Y. Ryu, T.P. Russell, C.J. Hawker, Block copolymer nanolithography: translation of molecular level control to nanoscale patterns, Adv. Mater. 21 (2009) 4769-4792.

[13] Y. Morikawa, S. Nagano, K. Watanabe, K. Kamata, T. Iyoda, T. Seki, Optical alignment and patterning of nanoscale microdomains in a block copolymer thin film, Adv. Mater. 18 (2006) 883-886.

[14] N. Demazy, C. Cummins, K. Aissou, G. Fleury, Non-Native Block Copolymer Thin Film Nanostructures Derived from Iterative Self-Assembly Processes, Advanced Materials Interfaces n/a 1901747.

[15] P.B. Smith, Oxygen-free, dry plasma process for polymer removal, Google Patents, 2001.

[16] M.A. Hillmyer, Nanoporous materials from block copolymer precursors, Block copolymers II, Springer2005, pp. 137-181.

[17] S. Hitz, R. Prins, Influence of template extraction on structure, activity, and stability of MCM-41 catalysts, J. Catal. 168 (1997) 194-206.

[18] J. Patarin, Mild Methods for Removing Organic Templates from Inorganic Host Materials, Angew. Chem. Int. Ed. 43 (2004) 3878-3880.

[19] M.D. Groner, F.H. Fabreguette, J.W. Elam, S.M. George, Low-Temperature Al2O3 Atomic Layer Deposition, Chem. Mater. 16 (2004) 639-645.

[20] R.Z. Waldman, D.J. Mandia, A. Yanguas-Gil, A.B.F. Martinson, J.W. Elam, S.B. Darling, The chemical physics of sequential infiltration synthesis—A thermodynamic and kinetic perspective, 151 (2019) 190901.

[21] J. Chai, J.M. Buriak, Using Cylindrical Domains of Block Copolymers To Self-Assemble and Align Metallic Nanowires, ACS Nano 2 (2008) 489-501.

[22] P.W. Majewski, A. Rahman, C.T. Black, K.G. Yager, Arbitrary lattice symmetries via block copolymer nanomeshes, Nature Communications 6 (2015) 7448.

[23] Y.-C. Tseng, Q. Peng, L.E. Ocola, D.A. Czaplewski, J.W. Elam, S.B. Darling, Etch properties of resists modified by sequential infiltration synthesis, Journal of Vacuum Science & Technology B, Nanotechnology and Microelectronics: Materials, Processing, Measurement, and Phenomena 29 (2011) 06FG01.

[24] S.I. Stupp, P.V. Braun, Molecular manipulation of microstructures: Biomaterials, ceramics, and semiconductors, Science 277 (1997) 1242-1248.

[25] G.M. Whitesides, J.P. Mathias, C.T. Seto, Molecular self-assembly and nanochemistry: a chemical strategy for the synthesis of nanostructures, Science 254 (1991) 1312-1319.

[26] S.-M. Lee, E. Pippel, U. Gösele, C. Dresbach, Y. Qin, C.V. Chandran, T. Bräuniger, G. Hause, M. Knez, Greatly Increased Toughness of Infiltrated Spider Silk, Science 324 (2009) 488-492.

[27] S. Mann, G.A. Ozin, Synthesis of inorganic materials with complex form, Nature 382 (1996) 313-318.

[28] K.E. Gregorczyk, D.F. Pickup, M.G. Sanz, I.A. Irakulis, C. Rogero, M. Knez, Tuning the tensile strength of cellulose through vapor-phase metalation, Chem. Mater. 27 (2014) 181-188.

[29] S.-M. Lee, E. Pippel, O. Moutanabbir, J.-H. Kim, H.-J. Lee, M. Knez, In situ Raman spectroscopic study of al-infiltrated spider dragline silk under tensile deformation, ACS applied materials & interfaces 6 (2014) 16827-16834.

[30] M. Biswas, J.A. Libera, S.B. Darling, J.W. Elam, New insight into the mechanism of sequential infiltration synthesis from infrared spectroscopy, Chem. Mater. 26 (2014) 6135-6141.

[31] Q. Peng, Y.C. Tseng, S.B. Darling, J.W. Elam, A Route to Nanoscopic Materials via Sequential Infiltration Synthesis on Block Copolymer Templates, Acs Nano 5 (2011) 4600-4606.

[32] A. Subramanian, N. Tiwale, C.-Y. Nam, Review of Recent Advances in Applications of Vapor-Phase Material Infiltration Based on Atomic Layer Deposition, JOM 71 (2019) 185-196.

[33] J. Frascaroli, E. Cianci, S. Spiga, G. Seguini, M. Perego, Ozone-Based Sequential Infiltration Synthesis of Al2O3 Nanostructures in Symmetric Block Copolymer, ACS Applied Materials & Interfaces 8 (2016) 33933-33942.

[34] H.C. Kim, S.M. Park, W.D. Hinsberg, Block Copolymer Based Nanostructures: Materials, Processes, and Applications to Electronics, Chem. Rev. 110 (2010) 146-177.

[35] A. Checco, A. Rahman, C.T. Black., Robust Superhydrophobicity in Large-Area Nanostructured Surfaces Defined by Block-Copolymer Self Assembly, Advanced Materials 26 (2014) 886.

[36] S.Y. Chou, P.R. Krauss, P.J. Renstrom, Imprint Lithography with 25-Nanometer Resolution, Science 272 (1996) 85-87.

[37] L. Cai, H. Shao, X. Hu, Y. Zhang, Reinforced and ultraviolet resistant silks from silkworms fed with titanium dioxide nanoparticles, ACS Sustainable Chemistry & Engineering 3 (2015) 2551-2557.

[38] D. Berman, S. Guha, B. Lee, J.W. Elam, S.B. Darling, E.V. Shevchenko, Sequential Infiltration Synthesis for the Design of Low Refractive Index Surface Coatings with Controllable Thickness, ACS Nano 11 (2017) 2521-2530.

[39] Y. She, E. Goodman, J. Lee, B.T. Diroll, M. Cargnello, E.V. Shevchenko, D. Berman, Block-Copolymer Assisted Synthesis of All Inorganic Highly Porous Heterostructures with Highly Accessible Thermally Stable Functional Centers, ACS applied materials & interfaces (2019).

[40] E. Barry, A.U. Mane, J.A. Libera, J.W. Elam, S.B. Darling, Advanced oil sorbents using sequential infiltration synthesis, Journal of Materials Chemistry A 5 (2017) 2929-2935.

[41] Y. She, J. Lee, B.T. Diroll, T.W. Scharf, E.V. Shevchenko, D. Berman, Accessibility of the pores in highly porous alumina films synthesized via sequential infiltration synthesis, Nanotechnology 29 (2018) 495703.

[42] G.T. Hill, D.T. Lee, P.S. Williams, C.D. Needham, E.C. Dandley, C.J. Oldham, G.N. Parsons, Insight on the Sequential Vapor Infiltration Mechanisms of Trimethylaluminum with Poly(methyl methacrylate), Poly(vinylpyrrolidone), and Poly(acrylic acid), The Journal of Physical Chemistry C 123 (2019) 16146-16152.

[43] G.N. Parsons, S.E. Atanasov, E.C. Dandley, C.K. Devine, B. Gong, J.S. Jur, K. Lee, C.J. Oldham, Q. Peng, J.C. Spagnola, P.S. Williams, Mechanisms and reactions during atomic layer deposition on polymers, Coord. Chem. Rev. 257 (2013) 3323-3331.

[44] Y. Wu, D. Döhler, M. Barr, E. Oks, M. Wolf, L. Santinacci, J. Bachmann, Atomic layer deposition from dissolved precursors, Nano Lett. 15 (2015) 6379-6385.

[45] M. Biswas, J.A. Libera, S.B. Darling, J.W. Elam, Kinetics for the Sequential Infiltration Synthesis of Alumina in Poly(methyl methacrylate): An Infrared Spectroscopic Study, Journal of Physical Chemistry C 119 (2015) 14585-14592.

[46] B.K. Barick, A. Simon, I. Weisbord, N. Shomrat, T. Segal-Peretz, Tin oxide nanostructure fabrication via sequential infiltration synthesis in block copolymer thin films, Journal of Colloid and Interface Science 557 (2019) 537-545.

[47] T. Kaufman-Osborn, E.A. Chagarov, A.C. Kummel, Atomic imaging and modeling of H2O2(g) surface passivation, functionalization, and atomic layer deposition nucleation on the Ge(100) surface, 140 (2014) 204708.

[48] J.W. Elam, D.A. Baker, A.J. Hryn, A.B.F. Martinson, M.J. Pellin, J.T. Hupp, Atomic layer deposition of tin oxide films using tetrakis(dimethylamino) tin, 26 (2008) 244-252.

[49] A.E. Short, S.V. Pamidi, Z.E. Bloomberg, Y. Li, M.D. Losego, Atomic layer deposition (ALD) of subnanometer inorganic layers on natural cotton to enhance oil sorption performance in marine environments, Journal of Materials Research 34 (2019) 563-570.

[50] A. Getsoian, J.R. Theis, W.A. Paxton, M.J. Lance, C.K. Lambert, Remarkable improvement in low temperature performance of model three-way catalysts through solution atomic layer deposition, Nature Catalysis (2019).

[51] R.W. Johnson, A. Hultqvist, S.F. Bent, A brief review of atomic layer deposition: from fundamentals to applications, Materials Today 17 (2014) 236-246.

[52] A.C. Jones, M.L. Hitchman, Chemical vapour deposition: precursors, processes and applications, Royal society of chemistry2009.

[53] C.-F. Huang, S.-W. Kuo, J.-K. Chen, F.-C. Chang, Synthesis and Characterization of Polystyrene-b-Poly(4-vinyl pyridine) Block Copolymers by Atom Transfer Radical Polymerization, Journal of Polymer Research 12 (2005) 449-456.

[54] R.A. Adomaitis, Estimating the thermochemical properties of trimethylaluminum for thin-film processing applications, Journal of Vacuum Science & Technology A: Vacuum, Surfaces, and Films 36 (2018) 050602.

[55] R.Z. Waldman, N. Jeon, D.J. Mandia, O. Heinonen, S.B. Darling, A.B.F. Martinson, Sequential Infiltration Synthesis of Electronic Materials: Group 13 Oxides via Metal Alkyl Precursors, Chemistry of Materials 31 (2019) 5274-5285.

[56] Y. Yu, Z. Li, Y. Wang, S. Gong, X. Wang, Sequential Infiltration Synthesis of Doped Polymer Films with Tunable Electrical Properties for Efficient Triboelectric Nanogenerator Development, Adv. Mater. 27 (2015) 4938-4944.

[57] E.C. Dandley, C.D. Needham, P.S. Williams, A.H. Brozena, C.J. Oldham, G.N. Parsons, Temperature-dependent reaction between trimethylaluminum and poly(methyl methacrylate) during sequential vapor infiltration: experimental and ab initio analysis, Journal of Materials Chemistry C 2 (2014) 9416-9424.

[58] M. Witt, H. Roesky, Organoaluminum chemistry at the forefront of research and development, Curr Sci 78 (2000) 410-430.

[59] Y. Xu, C.B. Musgrave, A DFT study of the Al2O3 atomic layer deposition on SAMs: effect of SAM termination, Chem. Mater. 16 (2004) 646-653.

[60] F. Fowkes, D. Tischler, J. Wolfe, L. Lannigan, C. Ademu-John, M. Halliwell, Acid–base complexes of polymers, Journal of Polymer Science: Polymer Chemistry Edition 22 (1984) 547-566.

[61] K. Ute, H. Ohnuma, I. Shimizu, T. Kitayama, Stereospecific Group Transfer Polymerization of Methyl Methacrylate with Lewis-Acid Catalysis—Formation of Highly Syndiotactic Poly (methyl methacrylate), Polym. J. 38 (2006) 999.

[62] B. Gong, G.N. Parsons, Quantitative in situ infrared analysis of reactions between trimethylaluminum and polymers during Al 2 O 3 atomic layer deposition, J. Mater. Chem. 22 (2012) 15672-15682.

[63] J.W. Elam, M. Biswas, S. Darling, A. Yanguas-Gil, J.D. Emery, A.B. Martinson, P.F. Nealey, T. Segal-Peretz, Q. Peng, J. Winterstein, New insights into sequential infiltration synthesis, ECS transactions 69 (2015) 147-157.

[64] A. Singh, W. Knaepen, S. Sayan, Z.e. Otell, B.T. Chan, J.W. Maes, R. Gronheid, Impact of sequential infiltration synthesis on pattern fidelity of DSA lines, SPIE Advanced Lithography, SPIE, 2015, pp. 7.

[65] M.J. Dewar, C. Jie, Mechanisms of pericyclic reactions: the role of quantitative theory in the study of reaction mechanisms, Acc. Chem. Res. 25 (1992) 537-543.

[66] Q. Peng, Y.C. Tseng, S.B. Darling, J.W. Elam, Nanoscopic Patterned Materials with Tunable Dimensions via Atomic Layer Deposition on Block Copolymers, Adv. Mater. 22 (2010) 5129-5133.

[67] J.W. Elam, M. Biswas, S.B. Darling, A. Yanguas-Gil, J.D. Emery, A.B.F. Martinson, P.F. Nealey, T. Segal-Peretz, Q. Peng, J. Winterstein, J.A. Liddle, Y.-C. Tseng, New Insights into Sequential Infiltration Synthesis, ECS Trans 69 (2015) 147-157.

[68] O.M.E. Ylivaara, X. Liu, L. Kilpi, J. Lyytinen, D. Schneider, M. Laitinen, J. Julin, S. Ali, S. Sintonen, M. Berdova, E. Haimi, T. Sajavaara, H. Ronkainen, H. Lipsanen, J. Koskinen, S.-P. Hannula, R.L. Puurunen, Aluminum oxide from trimethylaluminum and water by atomic layer deposition: The temperature dependence of residual stress, elastic modulus, hardness and adhesion, Thin Solid Films 552 (2014) 124-135.

[69] S.E. Potts, G. Dingemans, C. Lachaud, W.M.M. Kessels, Plasma-enhanced and thermal atomic layer deposition of Al2O3 using dimethylaluminum isopropoxide, [Al(CH3)2(μ-OiPr)]2, as an alternative aluminum precursor, Journal of Vacuum Science & Technology A: Vacuum, Surfaces, and Films 30 (2012) 021505.

[70] H.B. Profijt, S.E. Potts, M.C.M.v.d. Sanden, W.M.M. Kessels, Plasma-Assisted Atomic Layer Deposition: Basics, Opportunities, and Challenges, Journal of Vacuum Science & Technology A: Vacuum, Surfaces, and Films, Adv. Mater. Interf. 29 (2011) 050801: 050801 - 050826.

[71] E. Cianci, D. Nazzari, G. Seguini, M. Perego, Trimethylaluminum Diffusion in PMMA Thin Films during Sequential Infiltration Synthesis: In Situ Dynamic Spectroscopic Ellipsometric Investigation, 5 (2018) 1801016.

[72] B. Lee, J. Yoon, W. Oh, Y. Hwang, K. Heo, K.S. Jin, J. Kim, K.W. Kim, M. Ree, In-situ grazing incidence small-angle X-ray scattering studies on nanopore evolution in low-k organosilicate dielectric thin films, Macromolecules 38 (2005) 3395-3405.

[73] B.D. Lee, Y.H. Park, Y.T. Hwang, W. Oh, J. Yoon, M. Ree, Ultralow-k nanoporous organosilicate dielectric films imprinted with dendritic spheres, Nature Materials 4 (2005) 147-151.

[74] R.Z. Waldman, D. Choudhury, D.J. Mandia, J.W. Elam, P.F. Nealey, A.B.F. Martinson, S.B. Darling, Sequential Infiltration Synthesis of Al2O3 in Polyethersulfone Membranes, JOM 71 (2019) 212-223.

[75] E. Cianci, D. Nazzari, G. Seguini, M. Perego, Trimethylaluminum Diffusion in PMMA Thin Films during Sequential Infiltration Synthesis: In Situ Dynamic Spectroscopic Ellipsometric Investigation, Advanced Materials Interfaces 5 (2018) 1801016.

[76] J. Ren, L.E. Ocola, R. Divan, D.A. Czaplewski, T. Segal-Peretz, S. Xiong, R.J. Kline, C.G. Arges, P.F. Nealey, Post-directed-self-assembly membrane fabrication forin situanalysis of block copolymer structures, Nanotechnology 27 (2016) 435303.

[77] Y. She, J. Lee, B. Lee, B. Diroll, T. Scharf, E.V. Shevchenko, D. Berman, Effect of the Micelle Opening in Self-assembled Amphiphilic Block Co-polymer Films on the Infiltration of Inorganic Precursors, Langmuir 35 (2019) 796-803.

[78] S.-M. Lee, E. Pippel, O. Moutanabbir, I. Gunkel, T. Thurn-Albrecht, M. Knez, Improved Mechanical Stability of Dried Collagen Membrane after Metal Infiltration, ACS Applied Materials & Interfaces 2 (2010) 2436-2441.

[79] S. Choy, D.X. Oh, S. Lee, D.V. Lam, G. You, J.-S. Ahn, S.-W. Lee, S.-H. Jun, S.-M. Lee, D.S. Hwang, Tough and Immunosuppressive Titanium-Infiltrated Exoskeleton Matrices for Long-Term Endoskeleton Repair, ACS Applied Materials & Interfaces 11 (2019) 9786-9793.

[80] K.E. Gregorczyk, D.F. Pickup, M.G. Sanz, I.A. Irakulis, C. Rogero, M. Knez, Tuning the Tensile Strength of Cellulose through Vapor-Phase Metalation, Chemistry of Materials 27 (2015) 181-188.

[81] I. Azpitarte, A. Zuzuarregui, H. Ablat, L. Ruiz-Rubio, A. López-Ortega, S.D. Elliott, M. Knez, Suppressing the Thermal and Ultraviolet Sensitivity of Kevlar by Infiltration and Hybridization with ZnO, Chemistry of Materials 29 (2017) 10068-10074.

[82] C.-Y. Nam, A. Stein, Photodetectors: Extreme Carrier Depletion and Superlinear Photoconductivity in Ultrathin Parallel-Aligned ZnO Nanowire Array Photodetectors Fabricated by Infiltration Synthesis (Advanced Optical Materials 24/2017), 5 (2017) 1770119.

[83] E. Barry, J.A. Libera, A.U. Mane, J.R. Avila, D. DeVitis, K. Van Dyke, J.W. Elam, S.B. Darling, Mitigating oil spills in the water column, Environmental Science: Water Research & Technology 4 (2018) 40-47.

[84] W. Wang, F. Yang, C. Chen, L. Zhang, Y. Qin, M. Knez, Tuning the Conductivity of Polyaniline through Doping by Means of Single Precursor Vapor Phase Infiltration, 4 (2017) 1600806.

[85] W. Wang, C. Chen, C. Tollan, F. Yang, Y. Qin, M. Knez, Efficient and controllable vapor to solid doping of the polythiophene P3HT by low temperature vapor phase infiltration, Journal of Materials Chemistry C 5 (2017) 2686-2694.

[86] R.M. Dorin, H. Sai, U. Wiesner, Hierarchically Porous Materials from Block Copolymers, Chemistry of Materials 26 (2014) 339-347.

[87] H. Deng, L. Lin, M. Ji, S. Zhang, M. Yang, Q. Fu, Progress on the morphological control of conductive network in conductive polymer composites and the use as electroactive multifunctional materials, Prog. Polym. Sci. 39 (2014) 627-655.

[88] H. Yu, T. Kobayashi, H. Yang, Liquid-crystalline ordering helps block copolymer self-assembly, Adv. Mater. 23 (2011) 3337-3344.

[89] H. Yu, T. Kobayashi, G.-H. Hu, Photocontrolled microphase separation in a nematic liquid–crystalline diblock copolymer, Polymer 52 (2011) 1554-1561.

[90] D.H. Yi, C.-Y. Nam, G. Doerk, C.T. Black, R.B. Grubbs, Infiltration Synthesis of Diverse Metal Oxide Nanostructures from Epoxidized Diene–Styrene Block Copolymer Templates, ACS Applied Polymer Materials 1 (2019) 672-683.

[91] Y. She, J. Lee, B.T. Diroll, B. Lee, S. Aouadi, E.V. Shevchenko, D. Berman, Rapid Synthesis of Nanoporous Conformal Coatings via Plasma-Enhanced Sequential Infiltration of a Polymer Template, ACS Omega 2 (2017) 7812-7819.

[92] J. Kamcev, D.S. Germack, D. Nykypanchuk, R.B. Grubbs, C.-Y. Nam, C.T. Black, Chemically Enhancing Block Copolymers for Block-Selective Synthesis of Self-Assembled Metal Oxide Nanostructures, ACS Nano 7 (2013) 339-346.

[93] R.J. Klein, D.A. Fischer, J.L. Lenhart, Systematic Oxidation of Polystyrene by Ultraviolet-Ozone, Characterized by Near-Edge X-ray Absorption Fine Structure and Contact Angle, Langmuir 24 (2008) 8187-8197.

[94] E.C. Onyiriuka, The effects of high-energy radiation on the surface chemistry of polystyrene: A mechanistic study, J. Appl. Polym. Sci. 47 (1993) 2187-2194.

[95] N.C. Bigall, B. Nandan, E.B. Gowd, A. Horechyy, A. Eychmüller, High-Resolution Metal Nanopatterning by Means of Switchable Block Copolymer Templates, ACS Applied Materials & Interfaces 7 (2015) 12559-12569.

[96] J.M.G. Cowie, 3 - Block and Graft Copolymers, in: G. Allen, J.C. Bevington (Eds.), Comprehensive Polymer Science and Supplements, Pergamon, Amsterdam, 1989, pp. 33-42.

[97] Y. Chen, S. Huang, T. Wang, Z. Dong, H. Yu, Confined self-assembly enables stabilization and patterning of nanostructures in liquid-crystalline block copolymers, Macromolecules 52 (2019) 1892-1898.

[98] S. Huang, Y. Chen, S. Ma, H. Yu, Hierarchical Self-Assembly in Liquid-Crystalline Block Copolymers Enabled by Chirality Transfer, Angew. Chem. 130 (2018) 12704-12708.

[99] X. Gu, I. Gunkel, A. Hexemer, W. Gu, T.P. Russell, An In Situ Grazing Incidence X-Ray Scattering Study of Block Copolymer Thin Films During Solvent Vapor Annealing, 26 (2014) 273-281.

[100] J. Bang, U. Jeong, D.Y. Ryu, T.P. Russell, C.J. Hawker, Block Copolymer Nanolithography: Translation of Molecular Level Control to Nanoscale Patterns, 21 (2009) 4769-4792.

[101] X. Zhang, K.D. Harris, N.L.Y. Wu, J.N. Murphy, J.M. Buriak, Fast Assembly of Ordered Block Copolymer Nanostructures through Microwave Annealing, ACS Nano 4 (2010) 7021-7029.

[102] A. Rahman, P.W. Majewski, G. Doerk, C.T. Black, K.G. Yager, Non-native three-dimensional block copolymer morphologies, Nature Communications 7 (2016) 13988.

[103] P. Mansky, Y. Liu, E. Huang, T.P. Russell, C. Hawker, Controlling Polymer-Surface Interactions with Random Copolymer Brushes, Science 275 (1997) 1458-1460.

[104] H.-C. Kim, S.-M. Park, W.D. Hinsberg, Block copolymer based nanostructures: materials, processes, and applications to electronics, Chem. Rev. 110 (2009) 146-177.

[105] M.J. Fasolka, A.M. Mayes, Block copolymer thin films: physics and applications, Annual Review of Materials Research 31 (2001) 323-355.

[106] T. Hashimoto, J. Bodycomb, Y. Funaki, K. Kimishima, The Effect of Temperature Gradient on the Microdomain Orientation of Diblock Copolymers Undergoing an Order−Disorder Transition, Macromolecules 32 (1999) 952-954.

[107] P.W. Majewski, K.G. Yager, Millisecond Ordering of Block Copolymer Films via Photothermal Gradients, ACS Nano 9 (2015) 3896-3906.

[108] S.R. Nowak, K.G. Yager, Photothermally Directed Assembly of Block Copolymers, n/a 1901679.

[109] Y.-C. Tseng, Q. Peng, L.E. Ocola, J.W. Elam, S.B. Darling, Enhanced Block Copolymer Lithography Using Sequential Infiltration Synthesis, The Journal of Physical Chemistry C 115 (2011) 17725-17729.

[110] Y. Wang, Nondestructive Creation of Ordered Nanopores by Selective Swelling of Block Copolymers: Toward Homoporous Membranes, Acc. Chem. Res. 49 (2016) 1401-1408.

[111] J. Yin, X. Yao, J.-Y. Liou, W. Sun, Y.-S. Sun, Y. Wang, Membranes with Highly Ordered Straight Nanopores by Selective Swelling of Fast Perpendicularly Aligned Block Copolymers, ACS Nano 7 (2013) 9961-9974.

[112] H. Sai, K.W. Tan, K. Hur, E. Asenath-Smith, R. Hovden, Y. Jiang, M. Riccio, D.A. Muller, V. Elser, L.A. Estroff, S.M. Gruner, U. Wiesner, Hierarchical Porous Polymer Scaffolds from Block Copolymers, 341 (2013) 530-534.

[113] M.T. Keene, R. Denoyel, P.L. Llewellyn, Ozone treatment for the removal of surfactant to form MCM-41 type materials, Chem. Commun. (1998) 2203-2204.

[114] G. Büchel, R. Denoyel, P.L. Llewellyn, J. Rouquerol, In situ surfactant removal from MCM-type mesostructures by ozone treatment, J. Mater. Chem. 11 (2001) 589-593.

[115] C. Shi, O.L.G. Alderman, D. Berman, J. Du, J. Neuefeind, A. Tamalonis, J.K.R. Weber, J. You, C.J. Benmore, The Structure of Amorphous and Deeply Supercooled Liquid Alumina, Frontiers in Materials 6 (2019).

[116] J. Lee, A. Kuchibhotla, D. Banerjee, D. Berman, Silica nanoparticles as copper corrosion inhibitors, Materials Research Express 6 (2019) 0850e0853.

[117] K. Jacques, T. Joy, A. Shirani, D. Berman, Effect of Water Incorporation on the Lubrication Characteristics of Synthetic Oils, Tribology Letters 67 (2019) 105.

[118] J. Lee, D. Berman, Inhibitor or promoter: Insights on the corrosion evolution in a graphene protected surface, Carbon 126 (2018) 225-231.

[119] J. Lee, M. Atmeh, D. Berman, Effect of trapped water on the frictional behavior of graphene oxide layers sliding in water environment, Carbon 120 (2017) 11-16.

[120] A. Sinha, D.W. Hess, C.L. Henderson, Transport behavior of atomic layer deposition precursors through polymer masking layers: Influence on area selective atomic layer deposition, Journal of Vacuum Science & Technology B: Microelectronics and Nanometer Structures Processing, Measurement, and Phenomena 25 (2007) 1721-1728.

[121] L.E. Ocola, D.J. Gosztola, A. Yanguas-Gil, H.-S. Suh, A. Connolly, Photoluminescence of sequential infiltration synthesized ZnO nanostructures, Quantum Sensing and Nano Electronics and Photonics XIII, International Society for Optics and Photonics, 2016, pp. 97552C.

[122] R. Azoulay, N. Shomrat, I. Weisbord, G. Atiya, T. Segal-Peretz, Metal Oxide Heterostructure Array via Spatially Controlled–Growth within Block Copolymer Templates, 15 (2019) 1904657.

[123] H.B. Profijt, S.E. Potts, M.C.M.v.d. Sanden, W.M.M. Kessels, Plasma-Assisted Atomic Layer Deposition: Basics, Opportunities, and Challenges, 29 (2011) 050801.

[124] T. Prosek, M. Taube, F. Dubois, D. Thierry, Application of automated electrical resistance sensors for measurement of corrosion rate of copper, bronze and iron in model indoor atmospheres containing short-chain volatile carboxylic acids, Corros. Sci. 87 (2014) 376-382.

[125] R.H.G. Brinkhuis, A.J. Schouten, Thin-film behavior of poly(methyl methacrylates). 2. An FT-IR study of Langmuir-Blodgett films of isotactic PMMA, Macromolecules 24 (1991) 1496-1504.

[126] F. Namouchi, H. Smaoui, N. Fourati, C. Zerrouki, H. Guermazi, J.J. Bonnet, Investigation on electrical properties of thermally aged PMMA by combined use of FTIR and impedance spectroscopies, J. Alloys Compd. 469 (2009) 197-202.

[127] X. Li, J. Iocozzia, Y. Chen, S. Zhao, X. Cui, W. Wang, H. Yu, S. Lin, Z. Lin, From Precision Synthesis of Block Copolymers to Properties and Applications of Nanoparticles, Angew. Chem. Int. Ed. 57 (2018) 2046-2070.

[128] J. F. Ciebien, R.T. Clay, B.H. Sohn, R. E. Cohen, Brief review of metal nanoclusters in block copolymer films, New Journal of Chemistry 22 (1998) 685-691.

[129] M. Moshonov, G.L. Frey, Directing hybrid structures by combining self-assembly of functional block copolymers and atomic layer deposition: a demonstration on hybrid photovoltaics, Langmuir 31 (2015) 12762-12769.

[130] S. Obuchovsky, I. Deckman, M. Moshonov, T.S. Peretz, G. Ankonina, T. Savenije, G. Frey, Atomic layer deposition of zinc oxide onto and into P3HT for hybrid photovoltaics, Journal of Materials Chemistry C 2 (2014) 8903-8910.

[131] K.J. Dusoe, X. Ye, K. Kisslinger, A. Stein, S.-W. Lee, C.-Y. Nam, Ultrahigh elastic strain energy storage in metal-oxide-infiltrated patterned hybrid polymer nanocomposites, Nano Lett. 17 (2017) 7416-7423.

[132] H.I. Akyildiz, K.L. Stano, A.T. Roberts, H.O. Everitt, J.S. Jur, Photoluminescence Mechanism and Photocatalytic Activity of Organic–Inorganic Hybrid Materials Formed by Sequential Vapor Infiltration, Langmuir 32 (2016) 4289-4296.

[133] H.S. Suh, D.H. Kim, P. Moni, S. Xiong, L.E. Ocola, N.J. Zaluzec, K.K. Gleason, P.F. Nealey, Sub-10-nm patterning via directed self-assembly of block copolymer films with a vapour-phase deposited topcoat, Nat Nano advance online publication (2017).

[134] M. Callies, D. Quéré, On water repellency, Soft matter 1 (2005) 55-61.

[135] A. Marmur, The lotus effect: superhydrophobicity and metastability, Langmuir 20 (2004) 3517-3519.

[136] J.W. Leem, J.S. Yu, Wafer-scale highly-transparent and superhydrophilic sapphires for high-performance optics, Opt. Express 20 (2012) 26160-26166.

[137] L.E. Ocola, Y. Wang, R. Divan, J. Chen, Multifunctional UV and Gas Sensors Based on Vertically Nanostructured Zinc Oxide: Volume Versus Surface Effect, Sensors (Basel) 19 (2019) 2061.

[138] Y. Xie, C.A. Hill, Z. Xiao, H. Militz, C. Mai, Silane coupling agents used for natural fiber/polymer composites: A review, Composites Part A: Applied Science and Manufacturing 41 (2010) 806-819.

[139] J.Q. Xi, M.F. Schubert, J.K. Kim, E.F. Schubert, M.F. Chen, S.Y. Lin, W. Liu, J.A. Smart, Optical thin-film materials with low refractive index for broadband elimination of Fresnel reflection, Nature Photonics 1 (2007) 176-179.

[140] H.K. Raut, V.A. Ganesh, A.S. Nair, S. Ramakrishna, Anti-reflective coatings: A critical, in-depth review, Energy & Environmental Science 4 (2011) 3779-3804.

[141] P. Buskens, M. Burghoorn, M.C.D. Mourad, Z. Vroon, Antireflective Coatings for Glass and Transparent Polymers, Langmuir 32 (2016) 6781-6793.

[142] S. Guldin, P. Kohn, M. Stefik, J. Song, G. Divitini, F. Ecarla, C. Ducati, U. Wiesner, U. Steiner, Self-Cleaning Antireflective Optical Coatings, Nano Lett. 13 (2013) 5329-5335.

[143] E. Astrova, V. Tolmachev, Effective refractive index and composition of oxidized porous silicon films, Materials Science and Engineering: B 69 (2000) 142-148.

[144] J.-Q. Xi, M.F. Schubert, J.K. Kim, E.F. Schubert, M. Chen, S.-Y. Lin, W. Liu, J.A. Smart, Optical thin-film materials with low refractive index for broadband elimination of Fresnel reflection, Nature photonics 1 (2007) 176-179.

[145] A. Brovelli, G. Cassiani, Effective permittivity of porous media: A critical analysis of the complex refractive index model, Geophysical Prospecting 56 (2008) 715-727.

[146] M.D.G.F.H.F.J.W.E.S.M. George, Low-Temperature Al2O3 Atomic Layer Deposition, Chem Mater 16 (2004) 639-645

[147] R. Ruiz, H. Kang, F.A. Detcheverry, E. Dobisz, D.S. Kercher, T.R. Albrecht, J.J. de Pablo, P.F. Nealey, Density Multiplication and Improved Lithography by Directed Block Copolymer Assembly, 321 (2008) 936-939.

[148] J.H. Kim, H.M. Jin, G.G. Yang, K.H. Han, T. Yun, J.Y. Shin, S.-J. Jeong, S.O. Kim, Smart Nanostructured Materials based on Self-Assembly of Block Copolymers, 30 (2020) 1902049.

[149] C. Zhou, M. Dolejsi, S. Xiong, J. Ren, E.M. Ashley, G.S.W. Craig, P.F. Nealey, Combining double patterning with self-assembled block copolymer lamellae to fabricate 10.5 nm full-pitch line/space patterns, Nanotechnology 30 (2019) 455302.

[150] S.-H. Shin, Y.H. Kwon, Y.-H. Kim, J.-Y. Jung, M.H. Lee, J. Nah, Triboelectric charging sequence induced by surface functionalization as a method to fabricate high performance triboelectric generators, ACS nano 9 (2015) 4621-4627.

[151] C. Wang, L. Yin, L. Zhang, D. Xiang, R. Gao, Metal Oxide Gas Sensors: Sensitivity and Influencing Factors, 10 (2010) 2088-2106.

[152] L. Zhu, W. Zeng, Room-temperature gas sensing of ZnO-based gas sensor: A review, Sensors and Actuators A: Physical 267 (2017) 242-261.

[153] A. Kumar, Performance analysis of Zinc oxide based alcohol sensors, International Journal of Applied Science and Engineering Research 4 (2015) 427-436.

[154] Z. Chen, C. Lu, Humidity Sensors: A Review of Materials and Mechanisms, SENSOR LETTERS 3 (2005) 274-295.

[155] H. Farahani, R. Wagiran, M. Hamidon, Humidity Sensors Principle, Mechanism, and Fabrication Technologies: A Comprehensive Review, Sensors 14 (2014) 7881.

[156] R.J. Lazarowich, P. Taborek, B.-Y. Yoo, N.V. Myung, Fabrication of porous alumina on quartz crystal microbalances, J. Appl. Phys. 101 (2007) 104909.

[157] M. Rassoul, F. Gaillard, E. Garbowski, M. Primet, Synthesis and Characterisation of Bimetallic Pd–Rh/Alumina Combustion Catalysts, J. Catal. 203 (2001) 232-241.

[158] H. Gandhi, G. Graham, R.W. McCabe, Automotive exhaust catalysis, J. Catal. 216 (2003) 433-442.

[159] R. Anderson, K. Stein, J. Feenan, L. Hofer, Catalytic oxidation of methane, Industrial & Engineering Chemistry 53 (1961) 809-812.

[160] R.J. Farrauto, M. Hobson, T. Kennelly, E. Waterman, Catalytic chemistry of supported palladium for combustion of methane, Applied Catalysis A: General 81 (1992) 227-237.

[161] P. Henry, Palladium catalyzed oxidation of hydrocarbons, Springer Science & Business Media2012.

[162] H.-J. Freund, G. Meijer, M. Scheffler, R. Schlögl, M. Wolf, CO Oxidation as a Prototypical Reaction for Heterogeneous Processes, Angew. Chem. Int. Ed. 50 (2011) 10064-10094.

[163] C.E. Sing, J.W. Zwanikken, M. Olvera de la Cruz, Electrostatic control of block copolymer morphology, Nature Materials 13 (2014) 694-698.

[164] P.W. Majewski, K.G. Yager, Rapid ordering of block copolymer thin films, Journal of Physics: Condensed Matter 28 (2016) 403002.

[165] C. Tang, E.M. Lennon, G.H. Fredrickson, E.J. Kramer, C.J. Hawker, Evolution of Block Copolymer Lithography to Highly Ordered Square Arrays, 322 (2008) 429-432.

330x165mm (300 x 300 DPI)